

1

2 Sedimentary mechanisms of a modern banded iron formation on
3 Milos Island, Greece

4

5 ^{1,2}Ernest Chi Fru*, ³Stephanos Kiliias, ^{4,5}Magnus Ivarsson, ¹Jayne E. Rattray,
6 ³Katerina Gkika, ²Iain McDonald, ⁶Qian He, ¹Curt Broman

7

8 ¹Department of Geological Sciences, 10691, Stockholm University, Sweden.

9 ²School of Earth and Ocean Sciences, Cardiff University, Park Place, CF10 3AT,
10 Cardiff, UK.

11 ³Department of Economic Geology and Geochemistry, Faculty of Geology and
12 Geoenvironment, National and Kapodistrian University of Athens, Panepistimiopolis,
13 Zographou, 15784, Athens, Greece.

14 ⁴Department of Biology, University of Southern Denmark, Campusvej 55, Odense M,
15 DK5230, Denmark

16 ⁵Department of Palaeobiology, Swedish Museum of Natural History, Box 50007,
17 Stockholm, Sweden.

18 ⁶School of Chemistry, Cardiff University, Park Place, CF10 3AT, Cardiff, UK.

19

20 *Corresponding author

21 Tel: +44(0) 29 208 70058

22 Email: ChiFruE@cardiff.ac.uk

23

24 Short title: A modern banded iron formation

25 **Abstract.** An Early Quaternary shallow submarine hydrothermal iron formation (IF)
26 in the Cape Vani sedimentary basin (CVSB) on Milos Island, Greece, displays banded
27 rhythmicity similar to Precambrian banded iron formation (BIF). Field-wide
28 stratigraphic and biogeochemical reconstruction show two temporal and spatially
29 isolated iron deposits in the CVSB with distinct sedimentological character.
30 Petrographic screening suggests the photoferrothermic-like microfossil-rich IF
31 (MFIF), accumulated on a basement consisting of andesites, in a ~150 m wide basin,
32 in the SW margin of the basin. A banded non-fossiliferous IF (NFIF) sits on top of the
33 Mn-rich sandstones at the transition to the renowned Mn-rich formation, capping the
34 NFIF unit. Geochemical data relates the origin of the NFIF to periodic submarine
35 volcanism and water column oxidation of released Fe(II) in conditions predominated
36 by anoxia, similar to the MFIF. Raman spectroscopy pairs hematite-rich grains in the
37 NFIF with relics of a carbonaceous material carrying an average $\delta^{13}\text{C}_{\text{org}}$ signature of
38 ~-25‰. A similar $\delta^{13}\text{C}_{\text{org}}$ signature in the MFIF could not be directly coupled to
39 hematite by mineralogy. The NFIF, which post dates large-scale Mn deposition in the
40 CVSB, is composed primarily of amorphous Si (opal-SiO₂·nH₂O) while crystalline
41 quartz (SiO₂) predominates the MFIF. An intricate interaction between tectonic
42 processes, changing redox, biological activity and abiotic Si precipitation are
43 proposed to have collectively formed the unmetamorphosed BIF-type deposits in a
44 shallow submarine volcanic center. Despite the differences in Precambrian ocean-
45 atmosphere chemistry and the present geologic time, these formation mechanisms
46 coincide with those believed to have formed Algoma-type BIFs proximal to active
47 seafloor volcanic centers.

48
49
50
51

52 **Keywords:** Banded iron formation; BIF analog; Hydrothermal activity; Iron cycling;
53 Silica cycling.

54
55
56
57
58
59
60
61
62

64 **1 Introduction**

65 Banded iron formations (BIF) are chemical marine sediments of Precambrian origin
66 (Bekker et al., 2010). They contain at least 15% bulk Fe content and are characterized
67 by spectacular Fe-rich bands alternating with cherty Si-rich layers (James, 1954;
68 Gross, 1980; Simonson, 1985, 2003; Bekker et al., 2010). The interval spanning
69 3800-1800 million years ago (Ma), records intermittent but widespread BIF
70 deposition on all continents. After a ~1000 million year hiatus, BIFs reappeared
71 briefly during the Neoproterozoic Snowball Earth glaciations, ~750-550 Ma
72 (Hoffman et al., 1998; Bekker et al., 2010). BIFs are therefore considered a unique
73 feature of a distinct Precambrian ocean-atmosphere chemistry, compared to the fully
74 oxygenated Phanerozoic ocean and atmosphere (Bekker et al., 2010; Poulton and
75 Canfield, 2011).

76 Recently, a curious ~2.0 million year old Early Quaternary iron formation (IF)
77 displaying banded rhythmicity typical of BIFs, was serendipitously discovered in the
78 Cape Vani Sedimentary Basin (CVSB), Milos Island, Greece (Chi Fru et al., 2013,
79 2015). Before this discovery, Cape Vani was long known to host Mn oxide ores of
80 economic potential (Hein et al., 2000; Liakopoulos et al., 2001; Glasby et al., 2005;
81 Kiliias et al., 2007). Milos is an emergent volcano on the Hellenic Volcanic Arc
82 (HVA) where arc-volcanism and seafloor hydrothermal activity occur in thinned pre-
83 Alpine to Quaternary continental crust (Kiliias et al., 2013b) (Fig. 1). The first
84 reported IF from CVSB is unmetamorphosed and contains diverse microfossils
85 encrusted by hematite, with ferrihydrite proposed as a primary precursor mineral (Chi
86 Fru et al., 2013, 2015). Field stratigraphy, rare earth elements (REE), stable isotopes,
87 petrographic and microfossil studies point to microbial Fe deposition in a semi-

88 enclosed, shallow submarine basin under conditions analogous to those that formed
89 the Precambrian Algoma-type BIFs near volcanic centers (Chi Fru et al., 2015). These
90 earlier reports assumed a one-time basin-wide depositional event and a common
91 origin for all Fe-rich sedimentary rocks in the CVSB.

92 However, it remains unclear what sedimentary processes caused the distinct
93 deposition of the BIF-type rocks in a basin where Mn precipitation was apparently
94 widespread at various intervals. Moreover, it is not known how the Mn ores relate
95 temporally and spatially to Fe deposition in the ~1 km long CVSB. This knowledge
96 may provide clues to processes that triggered large-scale deposition of similar
97 Proterozoic Fe-Mn-rich deposits (Roy, 2006; Tsikos et al., 2010; Beukes et al., 2016).
98 Here, new sedimentological, petrological and biogeochemical analyses describe
99 cycles of periodic precipitation of shallow submarine Si and Fe-rich sedimentary
100 rocks and the plausible mechanisms that enabled their temporal and spatial separation
101 from the Mn deposits in the CVSB. The data reveal a much more complex
102 depositional system not only controlled by microbial Fe(II) oxidation as previously
103 proposed (Chi Fru et al., 2013, 2015), but suggests episodic submarine hydrothermal
104 activity coupled to changing redox conditions as a central mechanism in the formation
105 of the banded iron rocks.

106

107 **1.1 Geological setting**

108 K-Ar radiometric dating of biotite and amphiboles belonging to the dacitic/andesitic
109 lava domes flooring the CVSB basin gave an Upper Pliocene age of 2.38 ± 0.1 Ma
110 (Fytikas et al., 1986; Stewart and McPhie, 2006). Similarly, the presence of the
111 gastropod mollusk, *Haustator biplicatus* (Bronn, 1831), in the fossiliferous

112 sandstones/sandy tuffs hosting the Mn-rich deposit, indicate a biostratigraphic Upper
113 Pliocene to Lower Pleistocene age.

114 The geology, Fe and Mn mineralization of the CVSB have previously been
115 described in detail (Plimer, 2000; Hein et al., 2000; Liakopoulos et al., 2001;
116 Skarpelis and Koutles, 2004; Glasby et al., 2005; Stewart and McPhie, 2006; Kiliias,
117 2011; Alfieris and Voudouris, 2005; Alfieris, 2006; Alfieris et al., 2013; Chi Fru et
118 al., 2013, 2015; Papavassiliou et al., 2017). Briefly, the Milos IF is part of the CVSB,
119 a recently emergent sedimentary rift basin located NW of Milos Island, along the
120 HVA in the Aegean Sea, Greece (Fig. 1). It hosts a fossil analog of active shallow-
121 submarine hydrothermal activity on the coast of Milos Island (Dando et al., 1995).
122 The CVSB developed within a shallow-submarine rhyolitic-dacitic volcanic center,
123 filled up mainly by a ~35-50 m thick stratigraphic succession of
124 volcanoclastic/epiclastic sandstones/sandy tuffs, 35-40% of which is hydrothermally
125 mineralized by Mn oxides and barite (Hein et al., 2000; Liakopoulos et al., 2001;
126 Skarpelis and Koutles, 2004; Papavassiliou et al., 2017). Sedimentologic and fossil
127 data (trace, bivalves, echinoid and brachiopod fossils, together with microbially
128 induced sedimentary structures (e.g. Kiliias, 2011), suggest that most of the CVSB
129 sandstones/sandy tuffs hosting the Mn-rich deposit, are foreshore to shoreface shallow
130 submarine deposits, formed at a maximum depth of 200 mbsl. Over the last 0.8 Myr,
131 fluctuating water depths due to sea-level change of up to 120 m and volcanic edifice
132 building, has resulted in tectonic uplift of ~250 m (Papanikolaou et al., 1990). The
133 CVSB infill, currently 35 m above sea level, is tectonically bound by extrusive
134 rhyolite to the north, framed by elevated andesitic-dacitic centers, with the Cape Vani
135 and the Katsimoutis dacitic lava domes being the most prominent (Fig. 1).

136

137 **2 Methodology**

138 **2.1 Sample preparation**

139 Prior to mineralogical and geochemical analysis, exposed rock surface layers were
140 sawn and removed. GeoTech Labs (Vancouver, Canada) produced doubly polished
141 thin sections for mineralogical and textural analysis. Trace and rare earth element
142 analysis was performed after digestion of powdered samples with a mixture of acids
143 (HNO₃, HCl, HF) and heat until a clear solution was obtained (Chi Fru et al., 2013,
144 2015).

145

146 **2.2 Mineralogical analysis**

147 **2.2.1 X-Ray Diffraction (XRD) analysis**

148 A PANalytical Xpert-pro diffractometer at room temperature, 45 kV, 40 mA and
149 1.5406 Å wavelength and Cu-K α radiation and Ni-filter, was used for Powder X-Ray
150 Diffraction (PXRD) analysis. Samples were analyzed between 5-80° in step sizes of
151 0.017° with continuous mode scanning step time of 50.1650 s while rotating.

152

153 **2.2.2 Raman spectroscopy**

154 Raman analysis was performed with a confocal laser Raman spectrometer (Horiba
155 instrument LabRAM HR 800), equipped with a multichannel air-cooled (-70°C) 1024
156 x 256 pixel charge-coupled device (CCD) array detector as previously described (Chi
157 Fru et al. 2013, 2015). Spectral resolution was ~0.3 cm⁻¹/pixel. Accuracy was
158 determined by a repeated silicon wafer calibration standard at a characteristic Raman
159 line of 520.7 cm⁻¹.

160

161 **2.2.3 Transmission electron microscopy**

162 Specimens for transmission electron microscopy (TEM) were prepared from the
163 crushed rock specimen powder. This was followed by dry-dispersal onto a 300 mesh
164 holey carbon TEM Cu grid. Microscopy was conducted using a JEOL 2100 TEM
165 with a LaB₆ source in the School of Chemistry, Cardiff University, operated at
166 200kV. The X-EDS analysis was performed with an Oxford Instrument SDD detector
167 X-Max^N 80 T.

168

169 **2.2.4 Scanning electron microscopy**

170 Scanning Electron Microscopy-Energy Dispersive Spectroscopy (SEM-EDS) analysis
171 was done on a FEI QUANTA FEG 650 ESEM. Images were captured at 5 kV and
172 EDS data collected at 20 kV, using an Oxford T-Max 80 detector (Oxford
173 Instruments, UK). The analyses were performed in low vacuum to minimize surface
174 charging of uncoated samples. EDS elemental maps were collected for 30 min or until
175 the signal had stabilized, indicated by a clear distribution trend. The data were further
176 processed with the Oxford Aztec software.

177

178 **2.3 Geochemical analysis**

179 **2.3.1 Laser ablation ICP-MS and trace element analysis**

180 Laser Ablation-Inductively Coupled Plasma-Mass Spectrometry (LA-ICP-MS) was
181 performed at Cardiff University on polished thin sections. The LA-ICP-MS system
182 comprised a New Wave Research UP213 laser system coupled to a Thermo X Series
183 2 ICP-MS. The laser was operated using a frequency of 10 Hz at pulse energy of
184 ~5mJ for an 80µm diameter beam using lines drawn perpendicular to the layering and
185 at a movement speed of 26 microns sec⁻¹. Samples were analyzed in time resolved

186 analysis (TRA) mode using acquisition times of between 110 and 250 seconds;
187 comprising a 20 second gas blank, 80-220 second ablation and 10 second washout.
188 Dwell times varied from 2 msec for major elements to 35 msec for low abundance
189 trace elements. Blank subtraction was carried out using the Thermo Plasmalab
190 software before time resolved data were exported to Excel.

191 Separated and independently pulverized banded layers were digested by lithium
192 borate fusion followed by major, trace and rare earth element (REE) analyses using
193 ICP- Atomic Emission Spectrometry-Mass Spectrometry (ICP-AES-MS) and X-Ray
194 Florescence (XRF) at Bureau Veritas (Ankara). Geochemical data were compared
195 with previously published results for the more widely investigated Mn deposits (Hein
196 et al., 2000; Liakopoulos et al., 2001; Glasby et al., 2005).

197

198 **2.3.2 Isotope analysis**

199 C, N and S isotopic composition for the pulverized samples was determined as
200 previously described (Chi Fru et al., 2013, 2015), following combustion in a Carlo
201 Erba NC2500 analyzer and analyzed in a Finnigan MAT Delta V mass spectrometer,
202 via a split interface to reduce gas volume. Reproducibility was calculated to be better
203 than 0.15‰ for $\delta^{13}\text{C}$ and $\delta^{15}\text{N}$ and 0.2‰ for $\delta^{34}\text{S}$. Total C and N concentrations were
204 determined simultaneously when measuring the isotope ratios. The relative error was
205 <1% for both measurements. For carbon isotopic composition of organic carbon,
206 samples were pre-treated with concentrated HNO_3 prior to analysis.

207

208 **2.4 Organic geochemistry analysis**

209 Lipid biomarker and compound specific $\delta^{13}\text{C}$ analyses were executed on powdered
210 samples of sectioned bands from which exposed surface layers had been removed.

211 Modern sediments from Spathi Bay, 36°40'N, 24°31'E, southeast of Milos Island,
212 collected by push coring at 12.5 m below the seafloor were freeze-dried prior to
213 extraction to aid the identification of potential syngenetic biomarkers in the
214 Quaternary rocks. Between 4-6 g of ground samples were ultrasonically extracted
215 using 3×Methanol, 3×(1:1) Methanol:Dichloromethane (DCM), and 3×DCM and
216 extracts were combined and dried under N₂. Samples were subsequently re-dissolved
217 in DCM then methylated following the method of Ichihara and Fukubayashi (2010).
218 The resulting residue was silylated using, 20 µl pyridine and 20 µl (N, O-
219 Bis(trimethylsilyl)trifluoroacetamide) BSTFA and heated at 60°C for 15 min. Total
220 lipid extracts were analyzed using a Shimadzu QP 2010 Ultra gas chromatography
221 mass spectrometer (GC/MS). Separation was performed on a Zebron ZB-5HT column
222 (30 m x 0.25 mm x 0.10 µm) with a helium carrier gas flow at 1.5 ml min⁻¹. Samples
223 were injected splitless, onto the column at 40°C with the subsequent oven temperature
224 program ramped to 180°C at a rate of 15°C min⁻¹, followed by ramping to 325°C at a
225 rate of 4°C min⁻¹ and a final hold for 15 min. The MS was set to scan from 50 to 800
226 m/z with an event time of 0.70 sec and a scan speed of 1111 u/sec. All peaks were
227 background subtracted and identification confirmed using the NIST GC/MS library
228 and literature spectra. Contamination was not introduced into the samples, as blank
229 samples worked up concurrently with the rock fractions had results comparable to the
230 ethyl acetate instrument blank.

231

232 **2.5 Chemical weathering analysis**

233 Chemical index of alternation (CIA) was used to determine whether variations in
234 chemical weathering intensities would in addition to hydrothermal activity deliver
235 materials into the depositional basin from the continent, according to the

236 formula: $CIA = Al_2O_3 / (Al_2O_3 + CaO + Na_2O + K_2O) \times 100$. Extensively
237 applied, the CIA index reveals subtle changes in weathering fluxes (Nesbit and
238 Young, 1982; Maynard, 1993; Bahlburg & Dobrzinski, 2011), where increasing CIA
239 values generally indicate amplified chemical dissolution of rocks and selective release
240 of dissolvable CaO, Na₂O and K₂O into solution (Nesbit & Young, 1982; Maynard,
241 1993; Bahlburg & Dobrzinski, 2011). The broken rock particles enriched in the
242 poorly soluble Al₂O₃ fraction, settle to the seafloor as weathered sediments carrying a
243 chemical composition different from the source. In the absence of chemical
244 dissolution, no net chemical change is expected in the composition of sediments
245 compared to source and thus a low CIA index. CIA indices for detritus of 0-55, 55-75
246 and >75, are considered unweathered, unweathered to slightly weathered and
247 weathered to highly weathered, respectively (Nesbit & Young, 1982; Maynard, 1993;
248 Bahlburg & Dobrzinski, 2011).

249

250 **2.6 Redox analysis**

251 Redox depositional conditions were evaluated using the sequential Fe extraction
252 redox proxy (Poulton and Canfield, 2005, 2011), combined with REE composition of
253 the sediment (Planavsky et al., 2010).

254

255 **2.6.1 REE redox analysis**

256 REE data obtained as described in section 2.3.1 were normalized with the North
257 American Shale Composite (NASC) to maintain consistency with previous studies in
258 which NASC-normalized REE data (SN) were reported for the Milos BIF-type rocks
259 (Chi Fru et al., 2013, 2015). The data were further normalized with the Post Archean
260 Australian Shale (PAAS) (McLennan, 1989) standard for comparative purposes,

261 according to Bau and Dulski (1996). Ce anomalies, calculated from Ce/Ce^*
262 $(Ce_{(SN)}/0.5Pr_{(SN)} + 0.5La_{(SN)})$ and Pr/Pr^* $(Pr_{(SN)}/0.5Ce_{(SN)} + 0.5Nd_{(SN)})$ values, were
263 considered significant when Ce/Ce^* and Pr/Pr^* were less than and greater than 1,
264 respectively (Bau and Dulski et al., 1996; Planavsky et al., 2010).

265

266 **2.6.2 Sequential iron extraction redox analysis**

267 Analysis was performed on three representative MFIF samples and the six sectioned
268 bands of a typical NFIF sample using the method developed by Poulton and Canfield
269 (2005) and data interpreted accordingly (e.g., Canfield and Poulton, 2005, 2011;
270 Guilbaud et al. 2015; Sperling et al. 2015). Reagent blanks and geological standards
271 were used for data calibration.

272

273 **3 Results**

274 **3.1 Lithostratigraphy**

275 Sedimentary structures, grain-size, lateral facies variations, vertical stacking trends,
276 and key stratigraphic surfaces form the basis for facies analysis. Field-wide
277 sedimentological and lithostratigraphical mapping of the CVSB in the summer and
278 fall of 2014 enabled the assessment of the lateral and vertical coverage of the Milos
279 iron oxide-rich facies relative to the Mn-rich sandstones that dominate the Early
280 Quaternary sedimentary basin (Fig. 2). Six stratigraphic sections, representing marine
281 siliciclastic lithofacies sequences, were investigated along a ~1 km SW-NE trending
282 portion of the CVSB infill (Supplementary Figs 1-7). Sequence stratigraphy was
283 conducted on outcrops and vertical shafts and tunnels left behind by previous Mn
284 mining activity. Two of those sections; Section A located at $36^{\circ}44'17.85''N$,
285 $24^{\circ}21'17.72''E$ and Section B located at $36^{\circ}44'35.11''N$, $24^{\circ}21'11.25''E$, contain

286 stratigraphic units composed of layered, bedded, or laminated rocks that contain ≥ 15
287 % Fe, in which the Fe minerals are commonly interlayered with quartz or chert, in
288 agreement with the definition of BIFs (James, 1954; Gross, 1980; Bekker et al.,
289 2010). These IFs are descriptively referred to here as microfossiliferous iron
290 formation (MFIF) according to Chi Fru et al. (2013, 2015), and non-
291 microfossiliferous iron formation (NFIF) (this study), respectively (Fig. 2). The MFIF
292 and the NFIF occupy at most $\sim 20\%$ of the entire CVSB infill. The stratigraphy and
293 sedimentary lithofacies are illustrated below, using lithofacies codes modified after
294 Bouma (1962), Miall (1978, 1985), Lowe (1982), Mutti (1992) and Shanmugam
295 (2016).

296 Further field stratigraphic survey revealed considerable lithologic variability
297 within three fault-bounded volcanosedimentary sub-basins in the CVSB (Fig. 2),
298 which for the sake of simplicity are referred to as Basin 1—host of the MFIF; Basin
299 2—host of economic grade Mn ore; and Basin 3—host of the NFIF (Fig. 2). Each
300 section is framed by distinct marginal normal faults that strike in the NW-SE and NE-
301 SW to NNE-SSW directions, distinguishable by distinct lateral sedimentary facies
302 exhibiting unique vertical sequence stratigraphy (Fig. 2; Supplementary Figs 1-7).
303 Faulting in the CVSB is related to major geographical activation of extensional
304 structures at intervals that shaped Milos into a complex mosaic of neotectonic units
305 (Papanikolaou et al., 1990; van Hinsbergen et al., 2004).

306

307 **3.1.1 Section A (36°44'17.85''N, 24°21'17.72''E)**

308 Informally known as “Little Vani”, Section A is the type section containing the MFIF
309 at the base. It crops out in the W-SW edge of the CVSB (Figs 1 & 2) as a $\sim 6-7$ m high

310 cliff resting stratigraphically on submarine dacitic and andesitic lavas and domes.

311 This section extends laterally in the N-NE direction for an estimated 300–500 m.

312 Lithologically, the MFIF comprises laminated and massive fine-grained red
313 and white weathered ferruginous jaspelitic red chert layers (Chi Fru et al., 2013,
314 2015). The chert layers contain morphologically distinct Fe minerals dispersed in a
315 fine-grained siliceous matrix (Fig. 3), marked by the notable absence of pyrite and an
316 low S content (Chi Fru et al., 2013, 2015). Layers are tabular and typically laterally
317 continuous at scales of several meters, whereas wave and current structures (e.g.,
318 cross-lamination) are generally absent from the MFIF. The hematite-rich MFIF
319 laminae (Table 1) are built by massive encrustation of anoxygenic photoferrotrophic-
320 like microbial biofilms by precipitated Fe (Chi Fru et al., 2013). The base of the MFIF
321 outcrop, is visibly mineralized by black diffused bands/veins composed of Mn oxides
322 (Fig. 4 & Table 1).

323 A markedly ferruginous 2-3 m-thick section immediately overlies the MFIF,
324 comprising a distinct package of Fe-rich beds that transition up the section (Figs 4A
325 & 5). The lower 1-2 m consist of fine-grained sandstone beds that are well to
326 moderately sorted, containing a 20-40 cm thick portion dominated by plane parallel-
327 laminated sandstone/sandy tuff, massive to plane parallel-laminated sandstone/sandy
328 tuff, and massive sandstone/sandy tuff lithofacies (Fig. 5; Supplementary Fig. 1). The
329 fabric of these Fe-rich sandstone facies consists of sub-angular to sub-rounded and
330 100–600 μm fine to medium-grained volcanoclastic K-feldspar grains, making up to
331 75% of the total rock, with variable amounts of quartz and clay mineral grains.

332 The latter are overlain by a ~1-1.5 m sequence of poorly-sorted tabular clast-
333 supported pebble-to-cobble conglomerate beds with an erosional base, grading
334 upward into coarse to medium-grained sandstone/sandy tuff beds, with alternating

335 conglomerate cycles (Fig. 5), averaging 20-40 cm in thickness. The cobble/pebble
336 conglomerate clasts include intraformational volcanic rocks (dacite, andesite),
337 allochthonous volcanoclastic sandstone, and volcanoclastic microclasts (e.g. K-
338 feldspar), cemented by hematite (Fig. 5; Chi Fru et al., 2013; Kiliyas et al., 2013a).
339 Towards the westernmost edge of the “Little Vani” section, there is a facies change
340 from the graded pebbly conglomerate/sandy tuff rhythms to a predominantly Fe-rich
341 conglomerate bed (Fig. 6A), termed the conglomerate-hosted IF (CIF) in Chi Fru et
342 al. (2015), with a maximum thickness of ~0.5 m and a cobble size range of ~10 cm.
343 The Fe-rich conglomerate bed transitions upward into medium-grained pebbly reddish
344 ferruginous sandstones with thin volcanic rock and sandstone pebble lenses. This, in
345 turn, grades upwards into a very-fine-grained greenish glauconite-bearing plane
346 parallel-laminated sandstone to siltstone bed; characterized by soft-sediment
347 deformation structures, such as flame structures, convolute bedding and lamination
348 structures, loop bedding, load casts, and pseudonodules (Supplementary Figs 1-2).

349 The “Little Vani” section is eventually capped along an erosional surface by
350 an overlying 1-2 m thick section dominated by medium to fine-grained and
351 moderately to poorly-sorted reddish Fe-rich tabular sandstone beds, 10–40 cm thick,
352 topped by patchy sub-cm to cm-thick Mn-rich sandstones (Fig. 5; Supplementary Figs
353 1-2). Dominant lithofacies of the Fe-rich sandstone cap include planar and hummocky
354 cross-bedding, exhibiting bioturbation in places. The Fe-rich lithofacies cap is
355 laterally discontinuous, thinning out basinwards towards the N-NE, and can be
356 observed smoothly grading into a 1-2 m thick section composed of cm to sub-cm-
357 thick Mn-rich volcanoclastic sandstone lithofacies, described below in Section B. No
358 Fe-rich hydrothermal feeder veins are obvious in the MFIF. However, feeder veins

359 and Mn horizons can be observed to truncate laminations in the MFIF, and up through
360 the whole “Little Vani” section (e.g., Figs 4C & 5).

361 The MFIF rests directly on the submarine dacites-andesites that were
362 deposited in a relatively shallow submarine environment (Stewart and McPhie, 2006).
363 The fine-grained, finely laminated nature of the MFIF, and, the lack of evidence of
364 current or wave structures (e.g., symmetric ripples or hummocky cross-stratification),
365 coupled to the absence of volcanogenic detrital particles and intraclast breccia
366 structures, indicate a low energy sedimentation environment, marked by negligible
367 volcanic interference (e.g., Tice and Lowe, 2006; Konhauser et al., 2017). This
368 interpretation is supported by the observed enrichment of Fe in the MFIF; a
369 characteristic of relatively deeper water lithofacies (Konhauser et al., 2017). This
370 view is compatible with the proposition that hematite enrichment in the MFIF was
371 under the control of photoferrotrophic biofilms (Chi Fru et al., 2013) known to thrive
372 at lower light intensities (Kappler et al., 2005; Li et al., 2013; Konhauser et al., 2017).
373 The quiet environmental conditions would have ensured the formation of such stable
374 photoferrotrophic biofilms over extended periods of time that would have facilitated
375 the oxidation of hydrothermally released Fe(II) and the deposition of Fe(III) minerals.

376 In the overlying sandstone-conglomerate facies, the presence of sedimentary
377 structures indicative of wave action and currents (e.g. cross-stratification), that signify
378 rapid deposition during a high energy event, are consistent with a switch to a shallow-
379 submarine high energy environment (Stewart and McPhie, 2006; Chi Fru et al., 2015).
380 This shift in depositional environments may have been controlled by a combination of
381 submarine volcano-constructional processes, synvolcanic rifting and volcano-tectonic
382 uplift known to have formed the CVSB (Papanikolaou et al., 1990; Stewart and
383 McPhie, 2006).

384

385 **3.2 Section B (36°44'35.11''N, 24°21'11.25''E)**

386 This ~8-10 m thick fault-bounded stratigraphic section, here referred to as
387 “Magnus Hill”, is the type section that contains the NFIF (Figs 2 & 7; Supplementary
388 Figs 3-4). Two lithostratigraphic units—a lower unit A and an upper unit B—are
389 identified in this study. Unit A is made up of a lower sandstone facies that is ~4-5 m
390 thick, dominated by a Mn-oxide cement, overlain by reddish brown Fe-rich massive
391 sandstone beds (Fig. 8 & Supplementary Figs 3-4). The lower sandstone facies
392 represents the host of the main economic grade Mn oxide ores in the CVSB. This
393 constitutes part of a separate study devoted to the Mn ores and will not be dealt with
394 further here. Unit B, ~5 m thick, unconformably overlies unit A and comprises two
395 distinct packages of beds that transition up section from brownish pebble
396 conglomerate layers (0.5-1.0 m thick), in contact with the very fine-grained NFIF
397 deposit (Supplementary Fig. 8 & 9). The NFIF is capped by patchy cm-thick
398 crustiform Mn oxides. Bifurcating feeder veins composed of barite, quartz and Mn-
399 Fe-oxide minerals cut through the underlying sandstone beds (Supplementary Fig. 4).

400 The NFIF is composed of banded Fe-rich rocks (Fig. 7) exposed on the topmost
401 part of “Magnus Hill”. About 2-3 m thick, the NFIF consists of mm to sub-mm thick,
402 dark grey and brown Fe-rich bands, interbanded with reddish brown Si-rich layers
403 (Figs 7 & 9-11; Supplementary Figs 10-11). Sedimentary structures in the NFIF are
404 predominantly characterized by rhythmic mm to sub-mm thick laminations (e.g., Fig.
405 7). The iron oxide-rich bands made up mainly of hematite (Table 1 & Fig. 10C) are
406 typically composed of very fine-grained angular to sub-angular volcanic dust material
407 (i.e., fine volcanic ash with particle size under 0.063 mm, K-feldspar, tridymite and
408 cristobalite (Table 1) in an amorphous Si and crystalline hematite matrix (Fig. 12)).

409 The predominantly amorphous Si-rich bands are typically planar, finely laminated and
410 composed of microcrystalline to cryptocrystalline ferruginous chert.

411 The NFIF is directly overlain by a ~1 m thick laminated to massive well-
412 indurated, nodular-pisolitic ironstone bed (Fig. 8A, C & D) that locally preserves a
413 sub-horizontal fabric reflecting the bedding in the original sediment or contain various
414 ferruginous clasts such as fragments, nodules, pisoliths, and oololiths set in a hematite-
415 rich siliceous matrix (Fig. 8C). Scattered cm scale pisoliths display a crude concentric
416 internal layering, characterized by open and vermiform voids filled by cauliflower-
417 like Mn oxides overprint (Fig. 8D). The ferruginous NFIF lithofacies are interpreted
418 to represent the deepest water deposits in the “Magnus Hill” section based on its very
419 fine-grained sedimentary composition, fine laminations and a paucity of intraclast
420 breccias. These, combined with the lack of evidence for wave and current-formed
421 sedimentary structures (e.g., hummocky cross-stratification, trough and ripple cross-
422 stratification), indicate quiet water low energy sedimentation, likely below wave base
423 (Simonson and Hassler, 1996; Trendall, 2002; Krapež et al., 2003; Konhauser et al.,
424 2017).

425 We interpret that each graded Fe oxide-rich band of the NFIF (Supplementary
426 Fig. 9), represents an individual fallout deposit from a proximal pyroclastic eruption.
427 This interpretation is supported by normal grading in fine volcanic ash content that
428 reflects their likely origin as pyroclastic fallout deposits in an otherwise quiet water
429 setting. For example, tridymite is a stable SiO₂ polymorph formed at low pressures of
430 up to 0.4 GPa and at temperatures of ~870-1470 °C (Swamy et al., 1994; Morris et al.,
431 2016). The coincidence of tridymite formation with silicic volcanism is in agreement
432 with the widespread distribution of andesite, dacite and rhyolite lava domes in the
433 CVSB. For example, vapour phase production of tridymite, together with sanidine

434 mineralization (Fig. 10), are principally associated with rhyolite ash flow (Breitkreuz,
435 2013; Galan et al., 2013). Similarly, Cristobalite is a SiO₂ polymorph linked with high
436 temperature rhyolitic eruptions (Horwell et al., 2010). Finally, in situ carbonaceous
437 laminations are absent, suggesting that benthic microbial mat growth had no influence
438 on deposition of the NFIF. Ironstones overlying the NFIF are difficult to interpret
439 with the existing data, but may represent supergene ferruginous duricrust formation
440 resulting from subaerial weathering (Anand et al., 2002).

441

442 **3.3 Geochemistry**

443 **3.3.1 Geochemistry of the individual Fe-rich and Si-rich bands**

444 The SEM-EDS-electron micrographs of the NFIF thin sections reveal distinct Fe
445 bands and Si-rich layers alternating periodically with each other in a fine sediment
446 matrix as shown by the grain size (Figs 9 & 11 & Supplementary Figs 9-11). Laser
447 ablation ICP-MS line analysis indicates Si and Fe count intensities in the Milos BIF-
448 type rocks are comparable to the 2.5 Ga Precambrian BIF reference from the
449 Kuruman IF formation, Transvaal Supergroup, South Africa (Fig. 11). The laser
450 ablation ICP-MS data further show an inverse correlation between Fe and Si, the two
451 major elemental components of BIFs, irrespective of the thousands of millions of
452 years gap separating the Precambrian deposit from the recently formed Milos IF
453 formation.

454

455 **3.3.2 Mineralogy of the individual Fe-rich and Si-rich bands**

456 No other Fe(III)(oxyhydr)oxide minerals have been identified in the Cape Vani Fe-
457 rich facies different from hematite. Electron imaging of the NFIF Fe-rich bands
458 suggests Si, Al and K-rich phases are mostly associated with the volcanoclastic

459 material predominated by K-feldspar clasts (Fig. 9; Supplementary Figs 10 & 11). A
460 unique feature of the NFIF is that the hematite in the Fe-rich bands occurs in tight
461 association with a carbonaceous material (Fig. 10C), but not for the hematite in the
462 Fe-rich sandstones and in the MFIF. This is also the case for the CIF overlying the
463 MFIF. Hematite showing a fluffy texture and at times presenting as framboidal
464 particles, is sprinkled in the Si-rich cement containing traces of Al and K in the MFIF
465 rocks (Fig. 3). Lack of association of the framboidal-iron-rich particles with S,
466 following SEM-EDS analysis, rules out a pyrite affiliation and is consistent with the
467 non-sulfidic depositional model suggested by the sequential iron extraction redox
468 proxy (Fig. 13D). TEM analysis suggests platy nano-Fe oxide-rich particles
469 predominate in the NFIF and MFIF, confirmed by overlaid X-ray Energy Dispersive
470 spectra taken from selected areas (Fig. 12) and consistent with the XRD data showing
471 hematite in both samples. The platy hematite needles in the Milos BIF-type rocks are
472 morphologically, and by size, comparable to hematite needles reported in the ~2.5 Ga
473 Kuruman BIFs (Sun et al., 2015).

474 Unlike the Fe-rich bands, volcanoclasts in the Si-rich bands are much smaller
475 in size, occurring mainly as fine-grained (Supplementary Fig. 8-11), signifying
476 predominant precipitation during periods of weakened hydrothermal activity. The
477 SiO₂ matrix in both the MFIF and NFIF are fine-grained, occurring mainly as
478 amorphous opal in the NFIF (Figs 10B & 12A-B), whereas in the MFIF it is mainly
479 present as crystalline quartz (Fig. 12C-D). Relative concentrations of Al, K and Ti in
480 the samples are generally low, with bulk-measured concentrations in both the Si-/Fe-
481 rich bands, together with the SiO₂ and Fe₂O₃ content, covarying with continental crust
482 concentrations (Fig. 13A). Mn impregnation of the MFIF, preserved in the form of
483 replacement layers mostly identified as cryptomelane [K(Mn⁴⁺, Mn²⁺)₈O₁₆] (Table 1),

484 is below detection in the NFIF. Rare hausmannite ($\text{Mn}^{2+}\text{Mn}^{3+}_2\text{O}_4$) was detected in a
485 few cases in the MFIF (Fig. 10D).

486

487 **3.3.3 Hydrothermal versus continental weathering**

488 Trends of major elements from which CIA indices were calculated (Fig. 13B), covary
489 with those of the continental crust (Fig. 13A). Continental crust averages, refer to the
490 zone from the upper continental crust to the boundary with the mantle (Rudnick &
491 Gao, 2003). The calculated CIA indices average 52 with one outlier at 22 (Fig. 13B).
492 No distinct relationship could be established between the CIA indices and the
493 respective IFs or between the distinct alternating Si- and Fe-rich bands (Fig. 13).
494 Highly weathered clay minerals resulting from the chemical decomposition of
495 volcanic rocks, e.g., kaolinite representing maximum CIA values of 100 or 75-90 for
496 illite, are absent in the analyzed materials. The absence of carbonates in the rocks
497 strengthened the CIA indices, since CIA indices are expected to be lower when Ca
498 carbonates are present (Bahlburg and Dobrzinski, 2011). TiO_2 content, a detrital
499 proxy, is mostly constant and covaries with the CIA values (Fig. 13B), suggesting
500 little variability and limited continental weathering input. A fairly strong negative
501 linear correlation was found between SiO_2 and Fe_2O_3 values normalized to TiO_2
502 (inset, Fig. 13B).

503

504 **3.3.4 Redox reconstruction**

505 Redox reconstruction by sequential iron extraction (Poulton and Canfield, 2005,
506 2011; Guilbaud et al., 2015; Sperling et al., 2015) is consistent with deposition of
507 both the MFIF and NFIF facies beneath an anoxic, ferruginous bottom water body
508 (Fig. 13C-D). The shale-normalized REE values ($\text{REE}_{(\text{SN})}$) for both the MFIF and

509 NFIF are consistent with previous reports (Chi Fru et al., 2013, 2015), showing
510 patterns typical of marine sedimentary environments affected by hydrothermal
511 activity throughout Earth's history (e.g., Planavsky et al., 2010). There is a notable
512 absence of significant negative $Ce_{(SN)}$ anomalies for both the MFIF and NFIF (Fig.
513 14A-B). These observations are statistically corroborated by true Ce anomalies.
514 Further, the Eu/Eu* anomaly averages for the MFIF and NFIF and the distinct Fe-/Si-
515 rich bands, suggest a $\sim 2\times$ higher Eu/Eu* signal for the Si-rich bands relative to the
516 Fe-rich bands and between the MFIF and NFIF deposits (Fig. 14C). Average Pr and
517 Yb shale-normalized ratios (Pr/Yb*), a light vs. heavy REE enrichment proxy
518 (Planavsky et al., 2010), indicate similar depleted levels of light and heavy REE in
519 both the NFIF and MFIF, as well as in the Fe- and Si-rich bands (Fig. 14C). This
520 independent verification of the anoxic depositional conditions using the sequential Fe
521 proxy, suggests the NASC normalization protocol effectively captures the redox
522 depositional conditions of the Milos IF.

523

524 **3.4 Lipid biomarker distribution and chemotaxonomy**

525 Bulk $\delta^{13}C_{org}$ averaged -25.4‰ (SD: ± 0.22); -25.2‰ (± 0.26) for NFIF Fe-/Si-rich
526 bands and -25.6‰ (SD: ± 0.12) for bulk MFIF, respectively (Table 2). A fractionation
527 effect between the alternating Fe-/Si-rich layers ($\Delta^{13}C_{Fe-rich\ NFIF-Si-rich\ NFIF}$) is estimated
528 to be $\sim 0.23\text{‰}$ (SD ± 0.036), while $\Delta^{13}C_{Fe-rich\ NFIF-MFIF}$ and $\Delta^{13}C_{Si-rich\ NFIF-bulk\ MFIF}$, is
529 0.13‰ (SD: ± 0.11) and 0.36‰ (SD: ± 0.14), respectively. These differences are small
530 and within the margin of error of analysis, suggesting no strong distinction in $\delta^{13}C_{org}$
531 preserved in the different IFs and their various facies. They are interpreted to mean
532 similar carbon fixation processes operated during intervals of predominant Si and
533 Fe(III)(oxyhydr)oxides deposition in both IFs. Attempts to discriminate between these

534 environments by lipid biomarker analysis revealed mainly C₁₆-C₁₉ fatty acid methyl
535 esters (FAME) in the Fe-rich NFIF bands and in bulk MFIF, while the Si-rich NFIF
536 bands contain mainly C₁₂-C₂₁ FAMES, suggesting either selective preservation (lipid
537 recovery was lower in the Fe-rich MFIF bands) or shifts to different potential
538 biological populations during the deposition of the different layers. Preserved lipids
539 discriminate against typical microbial lipid biomarkers like hopanoids, while C₃ plant
540 FAME are detected in all studied materials (Fig. 15). However, the anaerobic bacteria
541 indicator, 10MeC_{16:0} FAME, was identified in a few bands.

542

543 **4 Discussion**

544 **4.1 Sedimentological processes**

545 The three sub-basin division of the CVSB is consistent with previous proposals
546 suggesting that sedimentation within the CVSB was characterized by active
547 synvolcanic rifting which must have been important in shaping basin topography and
548 the creation of sub-basin architecture (Papanikolaou et al., 1990; Stewart and McPhie,
549 2006; Liakopoulos et al., 2001; Papavassiliou et al., 2017). Moreover, this tectonic
550 regime would suggest that the location(s) of volcanism were continually changing
551 relative to the two stratigraphic sections, which themselves were also being affected,
552 i.e. changes in depositional water depth and sedimentation style or and/or that local
553 submarine or subaerial topographic highs impeded the lateral continuity of
554 sedimentary units (Stewart and McPhie, 2006). Chi Fru et al. (2015) have suggested
555 there is an upward deepening of the overall depositional setting recorded in the “Little
556 Vani” section, consistent with rifting during CVSB infilling time.

557 The CVSB floored by dacitic/andesitic lava domes and overlain by
558 volcanoclastic infill, dates back to Upper Pliocene-Lower Pleistocene. A complex

559 mosaic of lithologically diverse sedimentary units (blocks), confined by neotectonic
560 marginal faults, characterizes the CVSB (Fig. 2). The most pronounced of these faults
561 being the NW-trending Vromolimni-Kondaros fault (Papanikolaou et al., 1990) that
562 has been proposed as the trigger of the hydrothermal activity that deposited Mn ore in
563 the CVSB (Papanikolaou et al., 1990; Liakopoulos et al., 2001; Alfieris et al., 2013;
564 Papavassiliou et al., 2017). The stratigraphically tight coupling between Mn and Fe
565 deposition, linked by Fe oxide minerals in feeder-veins, and positive Eu anomalies
566 (Fig. 14) indicating vent-sourced Fe (Maynard, 2010), associate Fe mineralization to
567 fault-triggered hydrothermalism in the CVSB. This is consistent with models of
568 geothermal fluid circulation along fault lines as conduits for the Mn-rich fluids that
569 formed the Milos Mn ore deposit (Hein et al., 2000; Liakopoulos et al., 2001; Glasby
570 et al., 2005; Kiliyas, 2011; Papavassiliou et al., 2017). More importantly, the overall
571 complex neotectonic structure of the CVSB (Papanikolaou et al., 1990) would explain
572 the creation of restricted basins, with sedimentological, lithological and geothermal
573 conditions that enabled the development of unique biogeochemical circumstances in
574 which the NFIF and MFIF formed.

575 The presence of the three depositional basins is supported by the fact that the
576 sequence lithologies in each fault-bound unit are characterized exclusively by
577 occurrences of specific and variably thick stratigraphic packages that tend to be
578 absent in others. For example, the MFIF occurs restricted to basin 1 and the NFIF to
579 Basin 3. Basin 2 is further distinguished by 35-50 m thick interbedded ore-grade Mn-
580 mineralized and glauconitic sandstones/sandy tuffs, much less developed in Basins 1
581 and 3 (Fig. 2). The presence or absence of a stratigraphic sequence, together with its
582 thickness variation, are interpreted as a result of local syntectonic sediment formation
583 conditions in each basin as a result of block tectonic movements along fault lines

584 (Papanikolaou et al., 1990). It may also be attributed to unique basin scale water
585 column redox conditions (e.g. Bekker et al., 2010, and references therein), post-
586 depositional erosion and changing sea level stand (Cattaneo & Steel, 2000).

587 The lack of hydrothermal feeder veins or seafloor exhalative structures (i.e.,
588 chimneys) in the MFIF and NFIF lithologies, suggests that hydrothermal Fe(II) was
589 delivered by diffuse flow and that the Milos-IF formed on the seafloor.
590 Further, mineralisation of the MFIF is suggested to have occurred during two major
591 hydrothermal venting stages. The first produced the MFIF and the second
592 contaminated it with cryptomelane. Cryptomelane in the MFIF is therefore not a
593 replacement product of primary Mn oxides formed during the deposition of the MFIF,
594 because the anoxia prevailing in Basin 1 at the time (Figs 2 & 13C) would have
595 precluded the precipitation of Mn oxide minerals, hinting that a second phase
596 hydrothermal fluid emission rich in dissolved Mn, directly precipitated cryptomelane
597 from solution as a secondary mineral relative to the primary Fe(III)(oxyhydr)oxides in
598 the MFIF. This occurred during an episode when the MFIF deposit must have been
599 exposed to oxygenated fluids, most likely through mixing with seawater at depth,
600 indicated by the abundance of cryptomelane at the base of the MFIF. Our model for
601 cryptomelane precipitation in the MFIF is therefore different from the one suggesting
602 diagenetic transformation of primary Mn ores at Milos (Hein et al., 2001;
603 Liakopoulous et al., 2001; Papavassiliou et al. 2017).

604 Geomorphological/chemical reconfiguration orchestrated the deposition of the
605 NFIF in a deeper, small-restricted basin (Fig. 2). The deepening of Basin 3 is reflected
606 in the underlying graded conglomerate bed that exhibits an upward fining trend,
607 followed by transition into the fine-grain NFIF. The conglomerate bed may represent
608 rapid deposition during a high-energy event, i.e. storm or mass flow, whereas the

609 upward fining in the bed is better explained by the depositional mechanism losing
610 energy through time. These high-energy conditions must have ceased during the
611 deposition of the overlying NFIF, where we interpret that increased abundance of
612 finely laminated IF and decreased evidence of storm and/or mass flow reworking
613 reflects deepening conditions. The hypothesized deepening of Basin 3 is consistent
614 with the interpretation that active rifting was an important mechanism in the
615 formation of the CVSB (Papanikolaou et al., 1990).

616

617 **4.2 Formation Mechanism of The Milos BIFs**

618 **4.2.1 Paragenetic sequence**

619 It is stressed that the previously generalized model proposed for biological deposition
620 of the Milos IF, refers exclusively to parts of what is here designated as MFIF (Chi
621 Fru et al., 2013). The NFIF is banded, but does not display the typical microfossils
622 seen in the MFIF, where diffused microbanding apparently relates to the distribution
623 of microbial mats in thin sections (Chi Fru et al., 2013, 2015). The distinction of
624 microcrystalline quartz and amorphous silica phases in the MFIF and NFIF,
625 respectively, together with nano-crystalline hematite particles, suggests a primary
626 amorphous silica origin in both deposits, diagenetically transformed to quartz in the
627 MFIF. The difference in silica crystallinity between the IFs is concurrent with the
628 older age predicted for the MFIF relative to the NFIF, from reconstructed sequence
629 stratigraphy (Fig. 2). Hematite in BIFs is generally interpreted, based on
630 thermodynamic stability, to be a transformation product of various primary Fe(III)
631 minerals, with ferrihydrite often proposed as the primary water column precipitate
632 (Glasby and Schulz, 1999; Bekker et al., 2010; Johnson et al., 2008; Percoits et al.,
633 2009). It is thought that acidic pH yields mainly goethite while hematite is produced

634 at circumneutral pH (Schwertmann and Murad, 2007). The notable absence of
635 diagenetic magnetite and Fe carbonates (siderite and ankerite), point to negligible
636 coupling of primary Fe(III) oxyhydroxides reduction to organic matter oxidation by
637 the dissimilatory iron-reducing bacteria during burial diagenesis (Johnson et al.,
638 2008). Minor occurrence of iron-silicate phases (Chi Fru et al., 2015) indicates an
639 origin of the hematite precursor in seawater independent of the iron silicate proposed
640 in some cases (Fischer and Knoll, 2009; Rasmussen et al., 2013, 2014). The up to 50
641 wt% Fe content recorded in the Fe-rich bands, indicate that large amounts of
642 dissolved Fe(II) was intermittently sourced and deposited as primary Fe(III) minerals,
643 through various oxidative processes in the depositional basin.

644 Importantly, the CIA analysis does not support mass weathering and
645 mineralization of terrestrial Fe and Si, in agreement with the absence of rivers
646 draining into the CVSB (Chi Fru et al., 2013). The specific identification of plant
647 biolipids would at face value imply post-depositional contamination. However,
648 samples were sawn to remove exposed layers and only the laminated bands for the
649 NFIF were analyzed. Modern sediments from Spathi bay, located Southeast of Milos
650 Island where hydrothermal activity is presently occurring at 12.5 m below sea level,
651 revealed similar plant lipids as recorded in the Quaternary IF (Fig. 15G). Post-
652 depositional contamination with terrestrial plant lipids is therefore ruled out for the
653 idea that recalcitrant plant biomass probably entered the sediments via seawater
654 entrainment at the time of deposition (see Naden et al., 2005). This finding
655 necessitates the careful interpretation of bulk $\delta^{13}\text{C}_{\text{org}}$ values obtained from both the
656 modern and ancient Milos sediments, involving in situ and ex situ biological
657 contributions to $^{13}\text{C}_{\text{org}}$ fractionation by various known carbon fixation pathways
658 (Preuß et al., 1989; Berg et al., 2010).

659

660 **4.2.2 Tectono-sedimentary processes and band formation**

661 Fluctuation in hydrothermal activity is proposed to account for the banding in the
662 NFIF (Fig. 16), under redox depositional conditions inferred to be mainly reducing
663 for both investigated IFs, consistent with previous reports (Chi Fru et al., 2013, 2015).
664 Positive Eu anomalies indicate a hydrothermal origin for all but one of the sample
665 suite (Fig. 14A). However, statistically calculated Eu/Eu* anomalies ($Eu_{(SN)}/$
666 $(0.66Sm_{(SN)} + 0.33Tb_{(SN)})$) to correct for differences in Gd anomalies commonly
667 encountered in seawater (Planavsky et al., 2010) are in the range of 0.1-0.58,
668 averaging 0.42. The lack of statistically significant true negative Ce anomalies (Fig.
669 14B) supported by sequential Fe redox reconstruction (Fig. 3C-D; Planavsky et al.,
670 2010; Poulton and Canfield, 2005, 2011; Guilbaud et al., 2015; Sperling et al. 2015),
671 indicate a reducing depositional environment for both The MFIF and the NFIF.

672 CIA analyses traditionally provide relative information on contributions from
673 chemical weathering to sediment deposition, linked to operative hydrological and
674 climatological patterns on land. This information is often gleaned from ancient and
675 modern soils and from reworked siliclastic deposits in marine basins (Maynard, 1993;
676 Bahlburg & Dobrzinski, 2011). The calculated CIA values, however, are closer to the
677 range obtained for unweathered and or only minimally weathered volcanic rocks (e.g.,
678 Nesbitt & Young, 1982; Bahlburg & Dobrzinski, 2011), thus pointing to a
679 predominantly volcanic and/or hydrothermal provenance for the clastic sedimentary
680 materials in the IFs.

681 It has been suggested that the release of reduced submarine hydrothermal fluids
682 contributed towards maintaining water column anoxia during the deposition of
683 Precambrian BIFs (Bekker et al., 2010). The calculated Eu anomalies (Fig. 14) and

684 petrographic data showing volcanoclastic detritus (i.e., K-feldspar, sanidine, tridymite,
685 cristobalite) as key rock components are in agreement with a submarine hydrothermal
686 source for the investigated IFs. The coarse volcanoclastic detritus embedded in the Fe-
687 rich bands compared to the finer particles in the Si-rich layers, highlights rapid
688 oxidation of Fe(II) that coincided with periodic cycles of hydrothermal/volcanic
689 discharge of new materials into the water column. However, the fine-grained nature
690 of both the MFIF and NFIF deposits suggests that deposition likely occurred away
691 from where such activity was occurring or that volcanic/hydrothermal discharge of Fe
692 and Si was non-eruptive and disruptive. The Fe-rich bands repetitively revealed
693 hematite grains cementing the denser volcanoclastic fragments that gradually diminish
694 upwards into a zone of fine-grained hematite before transitioning into Si-rich bands
695 consisting mainly of finer volcanoclastic detritus. These observations provide three
696 valuable interpretational considerations for proposing a model for the formation of the
697 alternating Si and Fe-rich bands.

- 698 1. The Si and Fe oxides-rich bands are primary precipitates formed in the water
699 column, by a process in which the precipitation of amorphous Si occurred
700 during quiescent non-volcanic intervals, with the oxidation and precipitation
701 of reduced Fe intermittently introduced into the water column by
702 volcanic/hydrothermal activity to form the Fe oxides.
- 703 2. The repetitive zonation of distinct particle sizes, suggests density gradient
704 sedimentation that requires a water column-like environment, rather than
705 diagenetic alteration of pre-formed sediments by hydrothermal fluids.
- 706 3. The reducing depositional conditions do not support sediment diagenesis as
707 an alternative model for explaining the origin of the Milos IF. This is because
708 the oxidation of ferrous Fe supplied in reduced hydrothermal fluids, must

709 interact with a sizeable pool of oxygen, enabling microaerophilic bacterial
710 oxidation of ferrous iron to Fe(III)(oxyhydr)oxides (Johnson et al., 2008; Chi
711 Fru et al., 2012). Otherwise, light-controlled photoferrotrophy oxidizes
712 ferrous Fe to form ferric (oxyhydr)oxides in the absence of oxygen in the
713 photic zone of the water column (Weber et al., 2006).

714

715 **4.2.3 Biological involvement**

716 Hematite precipitation in the MFIF on microbial filaments (Chi Fru et al., 2013) was
717 previously used to propose a generalized basin-scale mechanism for the deposition of
718 Fe-rich rocks in Cape Vani. However, such filaments are absent in the NFIF, while
719 pure hematite grains are tightly bound to relics of an organic matter signal carrying a
720 maximum $\delta^{13}\text{C}_{\text{org}}$ signature of -25‰ (Table 2). Similar processes are recorded in
721 modern marine sediments where interactions between Fe and free organic matter has
722 been reported to enable the preservation up to 21.5wt% of total organic carbon over
723 geological time scales (Lalonde et al., 2012). Moreover, Fe generally traps and
724 preserves organic matter at redox interfaces (Riedel et al., 2013). The data appear to
725 suggest that the mechanism of Fe(III) (oxyhydr)oxide precipitation and preservation
726 varied between the two IFs. The photoferrotrophic-like filamentous fossils reported in
727 the MFIF (Chi Fru et al., 2013), are absent in the NFIF. This does not, however, rule
728 out the potential role of microbial involvement in Fe(II) oxidation, as diverse
729 microbial taxa carry out this process, several of which are non-filamentous (Chi Fru et
730 al., 2012). However, our data is insufficient to enable clear quantification of the levels
731 of abiotic vs. biotic contribution to Fe(II) oxidation in the NFIF. Nevertheless, the
732 inferred predominantly anoxic depositional conditions as explained above, together
733 with the identification of anaerobic bacteria biomarkers in the laminated bands,

734 intuitively favor significant contribution of anaerobic biological Fe(II) oxidation in
735 the precipitation of primary Fe(III)(oxyhydr)oxides in the NFIF. See Weber et al.,
736 2006, for a review of potential biological pathways to anaerobic Fe(II) oxidation.

737 Briefly, anaerobic microbial Fe(II) oxidation can proceed via nitrate reduction
738 and by photoferrotrophy to deposit Fe(III)(oxyhydr)oxides. These mechanisms have
739 been linked to microbial contribution to BIF formation (Weber et al., 2006; Kappler et
740 al., 2005) and also for the MFIF (Chi Fru et al., 2013). However, it is also possible
741 that microaerophilic neutrophilic Fe(II)-oxidizing bacteria likely played an important
742 role, assuming a depositional setting analogous to the Santorini caldera and Kolumbo
743 shallow submarine volcanoes, where such low-O₂-dependent microbial Fe(II)
744 oxidation has been identified to actively precipitate Fe(III)(oxyhydr)oxides (Kilias et
745 al., 2013b; Camilli et al., 2015). It appears that in the MFIF, precipitating
746 Fe(III)(oxyhydr)oxide minerals were bound and preserved free of organic carbon or
747 that such organic carbon was diagenetically degraded. As was previously shown,
748 Fe(III)(oxyhydr)oxides completely replaced the organic content of the filamentous
749 microfossils in the MFIF (Chi Fru et al., 2013).

750 The 10MeC_{16:0} FAME identified in the rocks has been reported in anaerobic
751 organisms coupling nitrite reduction to methane oxidation (Kool et al., 2012), in
752 sulfate and iron-reducing bacterial species such as *Desulfobacter*, *Desulfobacula*
753 (*Bühning et al., 2005; Dowling et al., 1986; Taylor and Parkes, 1983*), *Geobacter*,
754 *Marinobacter* and the marine denitrifier, *Pseudomonas nautical* (Kool et al., 2006;
755 *Bühning et al., 2005; Dowling et al., 1986*). It had previously been proposed that post-
756 depositional denitrification was a potential pathway for early organic matter removal,
757 justified by the low rock organic carbon and nitrogen content in the Milos BIF-type
758 rocks (Chi Fru et al., 2013, 2015; Table 2). Equally, the detected 10MeC_{16:0} FAME

759 has also been found in anaerobic oxidation of methane (AOM) communities (Alain et
760 al., 2006; Blumenberg et al., 2004), originating from sulfate reducing bacteria.
761 However, bulk sediment $\delta^{13}\text{C}_{\text{org}}$ of -20‰ does not reflect AOM activity that is
762 expected to produce bulk $\delta^{13}\text{C}_{\text{org}}$ values that are $\leq -30\text{‰}$. Low $10\text{MeC}_{16:0}$ FAME
763 concentrations frustrated attempts at acquiring its compound specific isotopic
764 signature to enable further biomolecular level reconstruction of active microbial
765 metabolisms to explain Fe deposition mechanisms.

766 It is nevertheless puzzling why potential microbial biomarkers typical of marine
767 or hydrothermal vent environments are hardly preserved in the rocks, given that
768 microfossil evidence indicates a vast community of diverse prokaryotic assemblages
769 in the adjacent MFIF (Chi Fru et al., 2013, 2015). Moreover, sediments of the modern
770 Milos hydrothermal system and elsewhere on the HVA, are ubiquitously colonized by
771 microbial life, characterized by the marked large-scale absence or low abundance of
772 higher life forms, including plants (Kilias et al., 2013b; Camilli et al., 2015; Oulas et
773 al., 2015). One possibility could be the discriminatory preservation of lipids related to
774 their selectivity and reactivity towards Fe(III)(oxyhydr)oxides and clays or different
775 pathways to diagenetic degradation (e.g., Canuel & Martens, 1996; Lü et al., 2010;
776 Riedel et al., 2013). As noted, the carbonaceous materials in the BIF-type NFIF rocks
777 occur in tight association with hematite.

778 Importantly, prokaryotic biomarkers are suggested to poorly preserve in these
779 young BIF analogs. This raises the possibility that this may provide an important
780 explanation for why lipid biomarkers are yet to be extracted from Precambrian BIFs.
781 Moreover, the data are compatible with the low C_{org} recorded in BIFs of all ages,
782 suggesting that the low C_{org} abundance may not be due to metamorphism as often
783 proposed (Bekker et al., 2010) or to C_{org} oxidation by dissimilatory iron reducing

784 bacteria to form ^{13}C -depleted siderite and ankerite during diagenesis (Johnson et al.,
785 2008; Bekker et al., 2010). The Milos BIF-type rocks are unmetamorphosed and lack
786 iron carbonate, yet have vanishingly low C_{org} levels similar to the ancient
787 metamorphosed BIFs. However, an alternative possibility is that the iron oxides may
788 have been reduced through biological oxidation of organic carbon, but carbonate
789 saturation was not reached (Smith et al., 2013).

790

791 **4.2.4 Mn layers and the deposition of the Si-Fe-rich facies**

792 Cryptomelane $[\text{K}(\text{Mn}^{4+}, \text{Mn}^{2+})_8\text{O}_{16}]$, which commonly occurs in oxidized Mn
793 deposits resulting from mineral replacement and as open space fillings (Papavassiliou
794 et al., 2016), is also common in the MFIF. This supports the idea of post-depositional
795 impregnation of the base of the MFIF by Mn-rich fluids. Microscopic analysis
796 supports the epigenetic origin of the Mn in the MFIF by revealing Mn oxides growing
797 along fractures, impregnating and replacing Fe minerals (Fig. 4B-F). The
798 macroscopically evident thinning out to disappearance of such Mn-rich horizons up
799 the MFIF, coupled by their development along microfractures emphasizes this
800 epigenetic origin. Mn is not a common feature of the NFIF, even though it sits on top
801 of a thin sandstone layer that is highly mineralized with Mn, locally forming the cap
802 of the main Mn ore at Cape Vani. The generally accepted view is that Mn-rich
803 hydrothermal fluids rose and mineralized the Cape Vani sandstones (Hein et al., 2000;
804 Liakopoulos et al., 2001; Glasby et al., 2005). Based on the stratigraphic location of
805 the MFIF, which pre-dates the Mn-rich sandstones, it is proposed that impregnation of
806 the MFIF by Mn was coeval with large-scale Mn ore mineralization of the Cape Vani
807 sandstones, implying the entire basin was likely oxygenated at the time. The lack of
808 Ce anomalies, confirmed by the sequential Fe extraction proxy data, suggests that

809 both the MFIF and the NFIF formed in anoxic settings. Similar data for the Mn oxides
810 have suggested formation in oxic settings (Glasby et al., 2005; Chi Fru et al., 2015).
811 This implies that Mn epigenetically replaced the MFIF, either because the basin was
812 tectonically uplifted into a high-energy oxygenated shallow water setting or that sea
813 level dropped, leading to partial metasomatism of the base of MFIF, when oxygenated
814 seawater mixed with reduced hydrothermal fluids and precipitated Mn. The lack of
815 significant Ce anomalies in the dataset, combined with the inferred deepening of basin
816 3 and the anoxic depositional conditions suggested by the sequential iron redox proxy,
817 further indicate that for the final deposition of the NFIF, an eventual deepening event
818 must have been triggered, resulting in deoxygenation of parts of the CVSB.

819 All of this is feasible with the three-basin-fault-bounded hypothesis as a
820 requirement for movement along fault lines in response to temporal tectonic
821 activation. The upward sequence transition from the Mn-rich sandstone facies,
822 through the pebbly conglomerate and the final termination in the overlying mud-
823 grained NFIF (Fig. 8B), reflect sedimentary features formed during multiple changes
824 in seawater levels (Cattaneo & Steel, 2000).

825 Uplifting is suggested by potential weathering of the NFIF to form the
826 ferruginous duricrust cap. Comparable ferruginous layers on Precambrian BIFs are
827 linked to pervasive subaerial chemical weathering, via the dissolution of the silica-
828 rich layers and precipitation of relatively stable Fe oxides in the spaces between more
829 resistant hematite crystals (e.g., Dorr, 1964; Shuster et al., 2012; Levett et al., 2016).
830 This collective evidence supports the existence of a geodynamic tectonic system
831 capable of producing shallow oxic to deeper anoxic basin conditions at different times
832 that would explain the existence of Mn and Fe oxide layers within the same
833 sedimentary sequence. For example, it is common knowledge that both Fe and Mn

834 oxides will precipitate in the presence of oxygen (Roy, 1997, 2006), with kinetic rates
835 usually being faster for the oxidation of reduced Fe than reduced Mn. In the Fe(II)-
836 rich conditions that prevail in anoxic settings, abiotic reactions between Fe(II) and Mn
837 oxides, produce Fe(III) leading to the dissolution of the Mn oxides to form reduced
838 Mn, implying Mn oxides should not accumulate (Dieke, 1985). Moreover, under these
839 conditions, biological precipitation of Fe(III) can occur rapidly, leaving dissolved Mn
840 in solution to be deposited when oxygen becomes available. Given that the
841 hydrothermal fluids of the Hellenic Volcanic Arc are commonly enriched in both
842 reduced Fe and Mn, the deposition of the MFIF and NFIF therefore implies there was
843 an existing mechanism that enabled the kinetic discrimination and deposition of the
844 oxides of Fe and Mn into separate settings, most likely dependent on prevailing redox
845 conditions. The accumulation of the ferruginous duricrust layer, overprinted by redox
846 sensitive Mn-nodules, above the NFIF indicates a new shallowing event might have
847 terminated the formation of the NFIF.

848

849 **4.2.5 Modern analogs on the HVA**

850 Mechanistic explanation for the development of potential stratified waters and
851 reducing conditions during the deposition of the Milos BIF is problematic. However,
852 evidence is available from present shallow submarine hydrothermal analogs in the
853 central part of the HVA, to which the CVSB belongs. These include:

854 (1) The crater floor of the Kolumbo shallow-submarine volcano (~600×1200
855 m), which rises 504 m from the crater floor to 18 m below sea level (Sigurdsson et al.,
856 2006; Kiliyas et al., 2013b).

857 (2) The N part of Santorini's submerged caldera walls, which rises from 390 m
858 below sea level to over 300 m above sea level (Druitt et al., 1999; Friedrich et al.,
859 2006; Nomikou et al., 2013; Camilli et al., 2015).

860 (3) The coastal embayments at the Kameni emergent volcanic islands in the
861 center of the Santorini caldera (Hanert, 2002; Nomikou et al., 2014; Robbins et al.,
862 2016).

863 The benthic waters within Kolumbo's crater potentially sustain O₂ depleted
864 conditions via stable CO₂-induced water column densification, and accumulation of
865 acidic water (pH ~5), extending ~10 m above the CO₂ venting crater floor (Kilias et
866 al., 2013b). This phenomenon is believed to lead not only to obstruction of vertical
867 mixing of bottom acidic water, but also to O₂ deprivation by precluding efficient
868 transfer of oxygenated surface seawater into the deeper crater layer. In addition,
869 diffuse CO₂ degassing is believed to be linked to the formation of Fe microbial mats
870 and amorphous Fe(III) oxyhydroxides on the entire Kolumbo crater floor (Kilias et
871 al., 2013b) and on the shores of Milos Island (Callac et al., 2017). Prerequisites for
872 the O₂-depleted conditions to happen are the closed geometry of the Kolumbo crater
873 and the virtually pure CO₂ composition of the released hydrothermal vent fluids that
874 produce O₂ stratification along a stable CO₂-pH gradient.

875 A similar scenario is reported for the Santorini caldera, where large (~5 m
876 diameter) CO₂-rich, acidic (pH, ~5.93) hydrothermal seafloor pools and flow
877 channels, develop within m-thick microbial Fe-mats on the seafloor slope at 250-230
878 m below sea level. Persistent hypoxia exists in these pools, representing concentrated
879 seafloor CO₂ accumulation centers generated by hydrothermal venting (Camilli et al.,
880 2015). Here, the dissolved O₂ content (~80 μM or less) in the pools is ~40 % depleted
881 relative to the surrounding ambient seawater (Camilli et al., 2015). These hypoxic

882 conditions are comparable to or even lower than those measured in the CO₂-rich
883 oxygen minimum zones of coastal oceans, relative to seawater existing in equilibrium
884 with atmospheric pO₂ and pCO₂ pressures (Paulmier et al., 2008, 2011; Franco et al.,
885 2014). These conditions enable strong redox stratification of the pool waters, in which
886 unique Si- and Fe-rich microbial mats are associated with amorphous opal and
887 Fe(III)(oxyhydro)oxides (Camilli et al., 2015). Importantly, the Fe microbial mats in
888 these CO₂-rich hypoxic pools are affiliated with specific microaerophilic Fe(II)-
889 oxidizing bacteria that accumulate Fe(III) oxyhydroxides (Camilli et al., 2015; Oulas
890 et al., 2015). These Fe bacteria are implicated in the deposition of the Precambrian
891 BIFs (Konhasuer et al., 2002; Planavsky et al., 2009; Bekker et al., 2010).

892 Hypoxia is also associated with the water column of the Fe(III)-rich coastal
893 embayments and their hydrothermal vents (≤ 1.0 m water depth), Kameni islands
894 (Hanert, 2002; Robbins et al., 2016 and references therein). Venting fluids are warm
895 (20-40 °C), acidic to circumneutral (pH 5.5-6.9), enriched in CO₂, Fe and Si
896 (Georgalas & Liatsikas, 1936, Boström et al., 1990; Handley et al., 2010; Robbins et
897 al., 2016). Water column stratification is expressed as decreasing O₂ with depth that is
898 positively related to Fe(III)(oxyhydr)oxide density and microaerophilic Fe(II)-
899 oxidizing bacterial prevalence (Hanert, 2002). Robbins et al. (2016) found that
900 Fe(III)-rich suspended particulate material in these “Fe bays” may be associated with
901 anoxia, extending up to the air-seawater interface, near the hydrothermal vents
902 (Hanert, 2002). They consist of ferrihydrite, goethite and microaerophilic Fe(II)-
903 oxidizers.

904 However, the biogeochemical occurrence of these phenomena within the
905 localized confines of the Santorini caldera and Kolumbo crater, may however be
906 difficult to achieve in ordinary shallow submarine hydrothermal settings, such as

907 those occurring on the coast of present day Milos. The same may be true for Tatum
908 Bay, where non-volcanic and unconfined diffuse hydrothermalism is widespread
909 (Dando et al., 1996; Pichler & Dix, 1996; Pichler & Veizer, 1999; Stüben et al., 1999;
910 Rancourt et al., 2001; Varnavas et al., 2005).

911 In the Kolumbo and Santorini hydrothermal fields, benthic pH averages 5.5 and
912 the deposition of carbonates is markedly absent (Kilias et al., 2013b, Camilli et al.,
913 2015; Robins et al., 2016). This conforms to observations in the MFIF and NFIF units
914 where carbonate mineralization is not detected, thereby suggesting a similar low pH
915 depositional environment for both the MFIF and NFIF. Ubiquitous
916 Fe(III)(oxyhydr)oxide precipitation and enriched Si content are prevalent in the CO₂-
917 rich-hypoxic shallow submarine Santorini caldera slope pools and the Kameni Fe-
918 embayments where sulfide precipitation is [restricted](#) (Camilli et al., 2015; [Robbins et](#)
919 [al., 2016](#)). Such sulfide-poor conditions are critical for the formation of BIFs (Bekker
920 et al., 2010).

921 A high Si and Fe(III)(oxyhydr)oxide content, absence of detectable carbonate
922 and Fe sulfide minerals, are hallmark characteristics of the Milos IF (Chi Fru et al.,
923 2013, 2015; Fig. 13C-D). This depositional situation is different, for example, from
924 the unconfined shallow submarine hydrothermal activity in Tatum Bay and Bahia
925 Concepcion, Baja California Sur state, Mexico, where authigenic carbonate
926 deposition is widespread (Canet et al., 2005; Pichler & Veizer, 1996, 2005).
927 Moreover, there is strong geological evidence that within volcanic crater
928 environments associated with high CO₂ emission, long-term water column redox
929 stratification is possible under these special conditions. For example, Lake Nyos, a
930 205 m deep volcanic crater lake in Cameroon, Central-West Africa, undergoes CO₂-
931 induced water column stratification, lasting several decades. The reducing bottom

932 waters contain low sulfate and elevated reduced Fe concentration, relative to the
933 oxidized surface water (Kling et al., 2005; Tiodjio et al., 2014; Ozawa et al., 2016).

934

935 **5 Concluding remarks**

936 This study shows the following new insights in light of what was previously known:

937 1. At least two distinct IFs (MFIF and NFIF) formed from hydrothermal mud,
938 within two localized sub-basins in the ~1 km-long CVSB, ~2.66-1.0 Myr ago,
939 controlled by local tectonism.

940 2. Local conditions of elevated and cyclic supply of ferrous Fe and dissolved Si,
941 accompanied by bottom water anoxic conditions in a localized reservoir
942 cutoff from the open ocean, can in principle allow the deposition of BIF-type
943 rocks in a modern marine setting. The rarity of this type of deposit, however
944 suggests that the conditions required for formation are not a frequent
945 occurrence under the present-day oxygen-rich atmosphere.

946 3. A working model that band formation may involve potential
947 Fe(III)(oxyhydr)oxide infilling of sediment pores and fractures during
948 diagenesis, is not supported by the data. In addition to the lack of observation
949 of such phenomena, as shown for replacive Mn mineralization, calculated Ce
950 and Eu anomalies, together with sequential iron extraction analysis, are
951 suggestive of anoxic depositional conditions likely induced by the release of
952 reduced hydrothermal/volcanic fluids into a cutoff sedimentary basin.

953 4. Both Fe(III)(oxyhydr)oxides and Mn oxides are precipitated in the presence
954 of oxygen. In its absence, the formation of Mn oxides is inhibited, while
955 photoferrotrophy in the anoxic photic zone of redox-stratified waters oxidizes
956 reduced Fe to Fe(III)(oxyhydr)oxides (Kappler et al., 2005; Weber et al.,

957 2006). Collectively, these observations provide an important feasible
958 mechanism for the knife sharp separation of the Mn oxide-rich ores in the
959 CVSB that are also Fe(III)(oxyhydr)oxide-rich, from the highly localized
960 MFIF and NFIF deposits that are Fe(III)(oxyhydr)oxide-rich but Mn oxide-
961 poor.

962 5. The mechanism of formation of the MFIF and NFIF therefore most likely
963 involved exhalative release of reduced hydrothermal/volcanic fluids into a
964 restricted and deoxygenated seafloor water column where the oxidation of
965 reduced Fe to Fe(III)(oxyhydr)oxides occurred, most likely by the activity of
966 photoferrotrophs (Chi Fru et al., 2013). Microaerophilic oxidation of Fe(II)
967 was likely critical, but that remains to be explored.

968 6. Episodic intensification of hydrothermal activity is identified as a main
969 mechanism for the formation of the millimetric BIF bands, adding to the
970 biological mechanism that was inferred from fossil records in the MFIF (Chi
971 Fru et al., 2013, 2015).

972 7. Abiotic Si precipitation was much slower relative to Fe(III) precipitation,
973 resulting in Fe-rich bands in the NFIF forming in association with large
974 fragments of volcaniclast and the Si-rich bands with finer Si grains.

975 8. A combination of the above processes produced pulses of Si and Fe in the
976 millimetric Si and Fe-rich bands in the NFIF.

977 9. Whether the rocks described here are analogs of Precambrian BIFs or not, and
978 whether the proposed formation mechanisms match those that formed the
979 ancient rocks, is opened to debate. However, there are many similarities to
980 proposed Precambrian BIF depositional models (e.g. Klien, 2005; Beukes and
981 Gutzmer, 2008; Smith et al., 2013; Bekker et al., 2010; Klein and Beukes,

982 1992). Importantly, the present study provides mechanisms by which rocks
983 with alternating Fe and Si-rich bands can be formed in the modern ocean.

984

985 *Data availability.* Data can be accessed by request from any of the authors

986

987 *Author contributions.* ECF, SK and MI designed the study. ECF, SK, KG and MI
988 performed fieldwork. ECF, JER, KG, IM and QH performed research. ECF, SK, KG,
989 MI, QH and JER interpreted data. ECF and SK wrote paper.

990

991 *Competing interests.* The authors declare that they have no conflict of interest.

992

993 *Acknowledgments.* Ariadne Argyraki, Nicole Posth, Nolwenn Callac and Eva Zygouri
994 are acknowledged field assistance during sampling and for stimulating intellectual
995 discussions. Special thanks to Christoffer Hemmingsson for contributing to the SEM
996 and XRD analyses. Christophe Brosson is acknowledged for his work on sequential
997 iron extraction. This work is funded by the European Research Council (ERC)
998 Seventh Framework Program (FP7) grant No. 336092 and the Swedish Research
999 Council grant No. 2012-4364.

1000

1001

1002

1003

1004

1005

1006

1007 **References**

- 1008 Alain, K., Holler, T., Musat, F., Elvert, M., Treude, T., and Kruger M.;
- 1009 Microbiological investigation of methane- and hydrocarbon-discharging mud
- 1010 volcanoes in the Carpathian Mountains, Romania. *Environ. Microbiol.*, 8, 574–
- 1011 590, 2006.
- 1012 Alfieris, D. and Voudouris, P.: Ore mineralogy of transitional submarine magmatic-
- 1013 hydrothermal deposits in W. Milos Island, Greece. *Bul. Acad. Sci.*, 43, 1–6, 2005.
- 1014 Alfieris, D.: Geological, geochemical and mineralogical studies of shallow submarine
- 1015 epithermal mineralization in an emergent volcanic edifice, at Milos Island (western
- 1016 side), Greece. PhD thesis, Department Geowissenschaften der Universität
- 1017 Hamburg, 2006.
- 1018 Alfieris, D., Voudouris, P., and Spry, P.: Shallow submarine epithermal Pb–Zn–Cu–
- 1019 Au–Ag–Te mineralization on western Milos Island, Aegean Volcanic Arc, Greece:
- 1020 Mineralogical, geological and geochemical constraints. *Ore Geol. Rev.*, 53, 159–
- 1021 180, 2013.
- 1022 Anand, R. R., Paine, M., and Smith, R.E.: Genesis, Classification and Atlas of
- 1023 Ferruginous Materials, Yilgarn Craton. CRC LEME Open File Report vol. 13,
- 1024 CSIRO Exploration and Mining, Perth, 2002.
- 1025 Bahlburg, H. and Dobrzinski, N.: A review of the Chemical Index of Alteration (CIA)
- 1026 and its application to the study of Neoproterozoic glacial deposits and climate
- 1027 transition. *Geol. Soc. London Mem.*, 36, 81–92, 2011.
- 1028 Bau, M. and Dulski, P.: Distribution of yttrium and rare- earth elements in the Penge
- 1029 and Kuruman Iron-Formations, oxidative scavenging of cerium on hydrous Fe
- 1030 oxide, Transvaal Supergroup, South Africa. *Precambrian Res.*, 79, 37–55, 1996.

- 1031 Berg, I.A., Kockelkorn, D., Ramos-Vera, W.H., Say, R.F., Zarzycki, J., Hügler, M.,
1032 Alber, B.E., and Fuchs, G.: Autotrophic carbon fixation in archaea. *Nat. Rev.*
1033 *Microbiol.*, 8, 447–460, 2010.
- 1034 Bekker, A., Slack J.F., Planavsky, N., Krapež B., Hofmann, A., Konhauser, K.O., and
1035 Rouxel, O.J.: Iron formation: The sedimentary product of a complex interplay
1036 among mantle, tectonic, oceanic, and biospheric processes. *Econ. Geol.*, 105, 467–
1037 508, 2010.
- 1038 Beukes, N.J., and Gutzmer, J.: Origin and Paleoenvironmental significance of major
1039 Iron Formations at the Archean-Paleoproterozoic boundary. *Econ. Geol.* 15, 5–47,
1040 2008.
- 1041 Beukes, N.J., Swindell, E.P.W., Wabo, H.: Manganese deposits of Africa, Episodes v.
1042 39, 285–317, 2016.
- 1043 Blumenberg, M., Seifert, R., Reitner, J., Pape, T., and Michaelis, W.: Membrane lipid
1044 patterns typify distinct anaerobic methanotrophic consortia. *Proc. Natl. Acad. Sci.*
1045 *U.S.A.*, 101, 11111–11116, 2004.
- 1046 Boström, K., Honnorez, J., Joensuu, O., and Rydell, H.: Chemistry of hydrothermal
1047 solutions in drill hole GPK-1, Palaea Kameni, Santorini, Greece. *Proceedings of*
1048 *the third international congress, Santorini, Greece.* 3, 257–260, 1990.
- 1049 Bronn, H.G.: *Übersicht der Fossilen Überreste in den tertiären subappenninischen*
1050 *Gebirgen. Italiens Tertiär-Gebilde und deren organische Einschlüsse.* Heidelberg
1051 pp. XII + 176 + 1 pl, 1831.
- 1052 Bouma, A.H.: *Sedimentology of Some Flysch Deposits.* Amsterdam, Elsevier, pp.
1053 168, 1962.

1054 Breikreuz, C.: Spherulites and lithophysae—200 years of investigation on
1055 hightemperature crystallization domains in silica-rich volcanic rocks. *Bull.*
1056 *Volcanol.*, 75, 1–16, 2013.

1057 Bühring, S.I., Elvert, M., and Witte, U.: The microbial community structure of
1058 different permeable sandy sediments characterized by the investigation of bacterial
1059 fatty acids and fluorescence in situ hybridization. *Environ. Microbiol.*, 7, 281–293,
1060 2005.

1061 Callac, N., Posth, N.R., Rattray, J.E., Yamoah, K.K.Y., Wiech, A., Ivarsson, M.,
1062 Hemmingsson, C., Kiliias, S.P., Argyraki, A., Broman, C., Skogby, H.,
1063 Smittenberg, R.H., and Chi Fru, E.: Modes of carbon fixation in an arsenic and
1064 CO₂-rich shallow hydrothermal ecosystem. *Sci. Rep.*, 7, 14708,
1065 doi:10.1038/s41598-017-13910-2, 2017.

1066 Camilli, R., Noumikou P., Escartin, J., Ridao, P., Mallios, A., Kiliias, S.P., Argyraki,
1067 A., and the Caldera Science Team: The Kallisti Limnes, carbon dioxide
1068 accumulating subsea pools. *Sci. Rep.*, 5, 12152, doi:10.1038/srep12152, 2015.

1069 Canuel, E.A. and Marten, C.S.: Reactivity of recently deposited organic matter:
1070 Degradation of lipid compounds near the sediment-water interface. *Geochim.*
1071 *Cosmo. Acta*, 60, 1793–1806, 1996.

1072 Canet, C., Prol-Ledesma, R.M., Torres-Alvarado, I., Gilg, H.A., Villanueva, R.E., and
1073 Cruz, R.L.S.: Silica-carbonate stromatolites related to coastal hydrothermal venting
1074 in Bahia Concepcion, Baja California Sur, Mexico. *Sed. Geol.*, 174, 97–113, 2005.

1075 Cattaneo, A. and Steel, R.J.: Transgressive deposits: a review of their variability.
1076 *Earth Sci. Rev.*, 62, 187–228, 2003.

1077 Chi Fru, E., Piccinelli, P., and Fortin, D.: Insights into the global microbial
1078 community structure associated with iron oxyhydroxide minerals deposited in the
1079 aerobic biogeosphere. *Geomicrobiol. J.*, 29, 587-610, 2012.

1080 Chi Fru, E., Ivarsson, M., Kiliyas, S.P., Bengtson, S., Belivanova, V., Marone, F.,
1081 Fortin, D., Broman, C., and Stampanoni, M.: Fossilized iron bacteria reveal a
1082 pathway to the origin banded iron formations. *Nat. Comm.*, 4, 2050 DOI:
1083 10.1038/ncomms3050, 2013.

1084 Chi Fru, E., Ivarsson, M., Kiliyas, S.P., Frings, P.J., Hemmingsson, C., Broman, C.,
1085 Bengtson, S. and Chatzitheodoridis, E.: Biogenicity of an Early Quaternary iron
1086 formation, Milos Island, Greece. *Geobiology*, 13, 225–44, 2015.

1087 Dando, P.R., Hughes, J.A., Leahy, Y., Niven, S.J., Taylor, L.J. and Smith, C.: Gas
1088 venting rates from submarine hydrothermal areas around the island of Milos,
1089 Hellenic Volcanic Arc. *Cont. Shelf Res.*, 15, 913–925, 1995.

1090 Dieke, P. Concentration of Mn and separation from Fe in sediments—I. Kinetics and
1091 stoichiometry of the reaction between birnessite and dissolved Fe(II) at 10°C.
1092 *Geochim. Cosmo. Acta*, 49, 1023–1033, 1985.

1093 Dorr, J.V.N.: Supergene iron ores of Minas Gerais, Brazil. *Econ. Geol.*, 59, 1203,
1094 1964.

1095 Dowling, N.J. E., Widdel, F., and White, D.C.: Phospholipid ester-linked fatty-acid
1096 biomarkers of acetate-oxidizing sulfate-reducers and other sulfide-forming
1097 bacteria. *J. Gen. Microbiol.*, 132, 1815–1825, 1986.

1098 Druitt, T. H. L., Edwards, R. M., Mellors, D. M., Pyle, R. S. J., Sparks, M., Lanphere,
1099 M. D., and Barreirio, B.; Santorini Volcano. *Geol. Soc. Mem. London*, 19, 165,
1100 1999.

1101 Fischer, W.W. and Knoll, A.H.: An iron shuttle for deepwater silica in Late Archean
1102 and early Paleoproterozoic iron formation. *Geol. Soc. Am. Bull.*, 121, 222–235,
1103 2009.

1104 Franco, A.C., Hernández-Ayón, J.M, Beier E., Garçon, V., Maske, H., Paulmier, A.,
1105 Färber-Lorda, J., Castro, R., and Sosa-Ávalos, R.: Air-sea CO₂ fluxes above the
1106 stratified oxygen minimum zone in the coastal region off Mexico. *J. Geophys. Res.*,
1107 119, 2923–2937, 2014.

1108 Friedrich, W.L., Kromer, B., Friedrich, M., Heinemeier, J., Pfeiffer, T., and Talamo,
1109 S.: Santorini eruption radiocarbon dated to 1627-1600 BC. *Science*, 312, 548–548,
1110 2006.

1111 Fytikas, M., Innocenti, F., Kolios, N., Manetti, P., Mazzuoli, R., Poli, G., Rita, F., and
1112 Villari, L.: Volcanology and petrology of volcanic products from the island of
1113 Milos and Neighbouring islets. *J. Vol. Geotherm. Res.*, 28, 297–317, 1986.

1114 Galan, L.D.P., Doval, M., La Iglesia, A., Soriano, J., and Chavez, L.: Occurrence of
1115 silica polymorphs nanocrystals in tuffaceous rocks, Province of the Mesa Central,
1116 Mexico, and their formation from subcritical Si-rich fluids. *Am. Mineral.*, 98, 977–
1117 985, 2013.

1118 Georgalas, G., and Liatsikas, N.: Die Historische entwicklung des Dafni-Ausbruches
1119 1925-1926. In *Santorin, Der Werdegang eines Inselvulkans und sein Ausbruch*
1120 *1925-1928, V. 2* (ed. Reck, H.). Verlag von Dietrich Reimer, Berlin, 1–96 pp,
1121 1936.

1122 Glasby, G.P. and Schulz, H.D.: Eh, pH diagrams for Mn, Fe, Co, Ni, Cu and As under
1123 seawater conditions: application of two new types of the Eh, pH diagrams to the
1124 study of specific problems in marine geochemistry. *Aquatic Geochem.*, 5, 227–
1125 248, 1999.

1126 Glasby, G.P., Papavassiliou, C.T., Mitsis, J., and Valsami-Jones, E.: The Vani
1127 manganese deposit, Milos island, Greece: A fossil stratabound
1128 Mn–Ba–Pb–Zn–As–Sb–W-rich hydrothermal deposit. *Develop. Volcanol.*, 7,
1129 255–291, 2005.

1130 Gromet, L.P., Dymek, R.F., Haskin, L.A., and Korotev, R.L.: The North American
1131 shale composit: Its compilation and major trace element characteristics. *Geochim.*
1132 *Cosmo. Acta*, 48, 2469–2482, 1984.

1133 Gross, G.A.: A classification of iron-formation based on depositional Environments.
1134 *Can. Min.*, 18, 215–222, 1980.

1135 Guilbaud, R., Poulton, S.W., Butterfield, N.J., Zhu, M., and Shields-Zou, G.A.: A
1136 global transition to ferruginous conditions during the early Neoproterozoic. *Nat.*
1137 *Geosci.* 8:466–470, 2015.

1138 Handley, K. M., Boothman, C., Mills, R. A., Pancost, R. D., and Lloyd, J. R.:
1139 Functional diversity of bacteria in a ferruginous hydrothermal sediment. *ISME J.*,
1140 4, 1193-1205, 2010.

1141 Hanert, H. H.: Bacterial and chemical iron oxide deposition in a shallow bay on
1142 Palaea Kameni, Santorini, Greece: microscopy, electron probe microanalysis, and
1143 photometry of in situ experiments. *Geomicrobiol. J.*, 19, 317–342, 2002.

1144 Hein, J. R., Stamatakis, M. G., and Dowling, J. S.: Trace metal-rich Quaternary
1145 hydrothermal manganese oxide and barite deposit, Milos Island, Greece. *Applied*
1146 *Earth Science: Trans. Inst. Min. Metal. Section B.*, 109, 67–76, 2000.

1147 Hoffman, P. F., Kaufman, A. J., Halverson, G. P., and Schrag, DP.: A Neoproterozoic
1148 Snowball Earth. *Science* 281, 1342-1346, 1998.

1149 Horwell, C.J., le Blond, S., Michnowicz, S. A. K. and Cressey, G.: Cristobalite in a
1150 rhyolitic lava dome: evolution of ash hazard. *Bull. Volcanol.* 72, 249-253, 2010.

1151 Ichihara, K. and Fukubayashi, Y.: Preparation of fatty acid methyl esters for gas-
1152 liquid chromatography. *J. Lipid Res.*, 51, 635–40, 2010.

1153 James, H. L.: Sedimentary facies of iron-formation. *Econ. Geol.*, 49, 235–293, 1954.

1154 Johnson, C. M., Beard, B. L., and Roden, E. E.: The iron isotope fingerprints of redox
1155 and biogeochemical cycling in modern and ancient Earth. *Ann. Rev. Earth Plan.*
1156 *Sci.*, 36, 457–493, 2008.

1157 Kappler, A., Pasquero, C., and Newman, D.K.: Deposition of banded iron formations
1158 by anoxygenic phototrophic Fe(II)-oxidizing bacteria. *Geology*, 33, 865–868,
1159 2005.

1160 Kiliyas, S. P., Detsi, K., Godelitsas, A., Typas, M., Naden, J., and Marantos, Y.:
1161 Evidence of Mn-oxide biomineralization, Vani Mn deposit, Milos, Greece. In:
1162 Proceedings of the ninth biennial Meeting of the Society for Geology Applied to
1163 Mineral Deposits, Dublin, Ireland. *Irish Assoc. Econ. Geol.* 1069–1072 pp, 2007.

1164 Kiliyas, S. P.: Microbial mat-related structures in the Quaternary Cape Vani
1165 manganese-oxide (-barite) deposit, NW Milos island, Greece. *Soc. Sed. Geol. Sp.*
1166 *Pub.*, 101, 97–110, 2011.

1167 Kiliyas, S. P., Chatzitheodoridis, E., and Lyon, I.: Molecular, chemical and
1168 morphological evidence for hematite biogenicity at the Quaternary Cape Vani Mn-
1169 (Ba-Fe) deposit, Milos, Greece. *Bull. Geol. Soc.*, 47, 834-842, 2013a.

1170 Kiliyas, P. S., Nomikou, P., Papanikolaou, D., Polymenakou, P. N., Godelitsas, A.,
1171 Argyraki, A., Carey, S., Gamaletsos, P., Mertzimekis, T. J., Stathopoulou, E.,
1172 Goettlicher, J., Steininger, R., Betzelou, K., Livanos, I., Christakis, C., Bell, K. C.:
1173 and Scoullou, M. New insights into hydrothermal vent processes in the unique
1174 shallow-submarine arc-volcano, Kolumbo (Santorini), Greece. *Sci. Rep.*, 3,
1175 doi:10.1038/srep02421, 2013b.

1176 Klein, C.: Some Precambrian banded iron-formations (BIFs) from around the world:
1177 Their age, geologic setting, mineralogy, metamorphism, geochemistry, and origins.
1178 *Am. Min.*, 90, 1473–1499, 2005.

1179 Kling, G. W., Evans, W. C., Tanyileke, G., Kusakabe, M., Ohba, T., Yoshida, Y., and
1180 Hell, J. V.: Degassing Lakes Nyos and Monoun: Defusing certain disaster. *Proc.*
1181 *Natl. Acad. Sci. U.S.A.*, 102, 14185–14190, 2005.

1182 Klein, C., and Beukes, N.J.: Time distribution, stratigraphy and sedimentologic
1183 setting, and geochemistry of Precambrian Iron Formation. In Schopf, J. W., and
1184 Klein, C.: *The Proterozoic Biosphere: A multidisciplinary study*, 139 – 146.
1185 Cambridge University Press, New York, 1992.

1186 Konhauser, K. O., Planavsky, N. J., Hardisty, D. S., Robbins, L. J., Warchola, T. J.,
1187 Haugaard, R., Lalonde, S. V., Partin, C. A., Oonk, P. B. H., Tsikos, H., and Lyons,
1188 T.W.: Iron formations: A global record of Neoproterozoic to Palaeoproterozoic
1189 environmental history. *Earth Sci. Rev.*, 172, 140-177, 2017.

1190 Krapež, B., Barley, M. E., Pickard, A. L.: Hydrothermal and resedimented origins of
1191 the precursor sediments to banded iron formations: Sedimentological evidence
1192 from the early Palaeoproterozoic Brockman Supersequence of Western Australia.
1193 *Sedimentology*, 50, 979-1011, 2003.

1194 Lalonde, K., Mucci, A., Quillet, A. and Gélinais, Y.: Preservation of organic matter in
1195 sediments promoted by iron. *Nature*, 483, 198–200, 2012.

1196 Levett, A., Gagen, E., Shuster, J., Rintoul, L., Tobin, M., Vongsvivut, J., Bamberg,
1197 K., Vasconcelos, P., and Southam, G.: Evidence of biogeochemical processes in
1198 iron duricrust formation. *J. South. Am. Earth Sci.*, 71, 131–142, 2016.

- 1199 Li, W., Czaja, A. D., Van Kranendonk, M. J., Beard, B. L., Roden, E. E., Johnson, C.
1200 M.: An anoxic, Fe(II)-rich, U-poor ocean 3.46 billion years ago. *Geochim. Cosmo.*
1201 *Acta*, 120, 65-79, 2013.
- 1202 Liakopoulos, A., Glasby, G. P., Papavassiliou, C. T. and Boulegue, J.: Nature and
1203 origin of the Vani manganese deposit, Milos, Greece: an overview. *Ore Geol. Rev.*,
1204 18, 181–209, 2001.
- 1205 Lü, D., Song, Q., and Wang, X.: Decomposition of algal lipids in clay-enriched
1206 marine sediment under oxic and anoxic conditions. *Chin. J. Oceanogr. Limnol.*, 28,
1207 131–143, 2010.
- 1208 Marschik, R., Bauer, T., Hensler, A.-S., Skarpelis, N., and Hölzl, S. Isotope
1209 Geochemistry of the Pb-Zn-Ba(-Ag-Au) Mineralization at Triades-Galana, Milos
1210 Island, Greece. *Res. Geol.*, 60, 335–347, 2010.
- 1211 Maynard, J. B.: Chemistry of modern soils as a guide to interpreting Precambrian
1212 Paleosols. *J. Geol.*, 100, 279–289, 1993.
- 1213 Maynard, J. B.: The chemistry of manganese ores through time: a signal of increasing
1214 diversity of earth-surface environments. *Econ. Geol.*, 105, 535–552, 2010.
- 1215 McLennan, S.B.: Rare earth elements in sedimentary rocks. Influence of provenance
1216 and sedimentary processes. In: B.R. Lipin and G.A. McKay (Editors),
1217 *Geochemistry and Mineralogy of the Rare Earth Elements*. Mineralogical Society
1218 of America, Washington, pp. 169-200, 1989.
- 1219 Miall, A. D. Lithofacies types and vertical profile models in braided river deposits.
1220 *Can. Soc. Pet. Geol. Mem.*, 5, 597–604, 1978.
- 1221 Miall, A. D.: Architectural element analysis: a new method of facies analysis applied
1222 to fluvial deposits. *Earth Sci. Rev.*, 22, 261e308, 1985.

1223 Morris, R. V., Vaniman, D. T., Blake, D. F., Gellert, R., Chipera, S. J., Rampe, E. B.,
1224 Ming, D. W., Morrison, S. M., Downs, R. T., Treiman, A. H., Yen, A. S.,
1225 Grotzinger, J. P., Achilles, C. N., Bristow, T. F., Crisp, J. A., Des Marais, D. J.,
1226 Farmer, J. D., Fendrich, K. V., Frydenvang, J., Gradd, T. G., Morookian, J-M.,
1227 Stolper, E. M. and Schwenzer, S. P.: Silicic volcanism on Mars evidenced by
1228 tridymite in high-SiO₂ sedimentary rock at Gale crater. *Proc. Natl. Acad. Sci.*
1229 *U.S.A.*, 113, 7071–7076, 2016.

1230 Mutti, E.: *Turbidite Sandstones*. Agip Spe. Pub., 275 pp, 1992.

1231 Nesbitt, H. W. and Young, G. M.: Early Proterozoic climates and plate motions
1232 inferred from major element chemistry of lutites. *Nature*, 199, 715–717, 1982.

1233 Nomikou, P., Papanikolaou, D., Alexandri, M., Sakellariou, D., and Rousakis, G.:
1234 Submarine volcanoes along the Aegean volcanic arc. *Tectonophysics*, 597–598,
1235 123–146, 2013.

1236 Nomikou, P., Parks, M. M., Papanikolaou, D., Pyle, D. M., Mather, T. A., Carey, S.,
1237 Watts, A. B., Paulatto, M., Kalnins, M.L., Livanos, I., and Bejelou, K.: The
1238 emergence and growth of a submarine volcano: The Kameni islands, Santorini
1239 (Greece). *Geo. Res. J.*, 1, 8–18, 2014.

1240 Ozawa, A., Ueda, A., Fantong, W. Y., Anazawa, K., Yoshida, Y., Kusakabe, M.,
1241 Ohba, T., Tanyileke, G., and Hell, J.V. Rate of siderite precipitation in Lake Nyos,
1242 Cameroon. *Geol. Soc. London Sp. Pub.*, 437, doi.org/10.1144/SP437.13, 2016.

1243 Papanikolaou, D., Lekkas, E., and Syskakis, D.: Tectonic analysis of the geothermal
1244 field of Milos Island. *Bull. Geol. Soc. Greece*, 24, 27–46, 1990.

1245 Papavassiliou, K., Voudouris, P., Kanellopoulos, C., Glasby, G., Alfieris, D., and
1246 Mitsis, I.: New geochemical and mineralogical constraints on the genesis of the
1247 Vani hydrothermal manganese deposit at NW Milos island, Greece: Comparison

1248 with the Aspro Gialoudi deposit and implications for the formation of the Milos
1249 manganese mineralization. *Ore Geol.*, 80, 594–611, 2017.

1250 Paulmier, A., Ruíz-Pino, D., and Garçon, V.: The oxygen minimum zone (OMZ) off
1251 Chile as intense source of CO₂ and N₂O, *Cont. Shelf. Res.*, 28, 2746–2756, 2008.

1252 Paulmier, A., Ruiz-Pino, D., and Gaçon, V.: CO₂ maximum in the oxygen minimum
1253 zone (OMZ). *Biogeosciences*, 8, 239–252. doi:10.5194/bg-8-239-2011, 2011.

1254 Percoits, E., Gingras, M. K., Barley, M. E., Kapper, A., Posth, N. R., and Konhauser,
1255 K.O.: Petrography and geochemistry of the Dales Gorge banded iron formation:
1256 Paragenetic sequence, source and implications for palaeo-ocean chemistry. *Pre.*
1257 *Res.*, 172, 2009.

1258 Pichler, T. and Dix, G. R. Hydrothermal venting within a coral reef ecosystem,
1259 Ambitle Island, Papua New Guinea. *Geology*, 50, 435–438, 1996.

1260 Pichler, T. and Veizer, J.: Precipitation of Fe(III) oxyhydroxide deposits from
1261 shallow-water hydrothermal fluids in Tutum Bay, Ambitle Island, Papua New
1262 Guinea. *Chem. Geol.*, 162, 15–31, 1999.

1263 Pichler, T. and Veizer, J. The precipitation of aragonite from shallow-water
1264 hydrothermal fluids in a coral reef, Tutum Bay, Ambitle Island, Papua New
1265 Guinea. *Chem. Geol.*, 207, 317–45, 2004.

1266 Planavsky, N., Rouxel, O., Bekker, A., Shapiro, R., Fralick, P., and Knudsen, A.:
1267 Iron-oxidizing microbial ecosystems thrived in late Paleoproterozoic redox-
1268 stratified oceans. *Earth Plan. Sci. Letts.*, 286, 2307–242, 2009.

1269 Planavsky, N. J., Bekker, A., Rouxel, O. J., Kamber, B., Hofmann, A., Knudsen, A.
1270 and Lyons T. W.: Rare earth element and yttrium compositions of Archean and
1271 Paleoproterozoic Fe formations revisited: New perspectives on the significance
1272 and mechanisms of deposition. *Geochim. Cosmo. Acta*, 74, 6387–6405, 2010.

1273 Plimer, I. *Milos Geologic History*. Koan Publishing House, Athens, Greece. 261 pp,
1274 2000.

1275 Poulton, S.W., and Canfield, D.E.: Development of a sequential iron extraction
1276 procedure for iron: implications for iron partitioning in continentally derived
1277 particles. *Chem. Geol.* 2014, 209–221, 2005.

1278 Poulton, S.W. and Canfield, D.E.: Ferruginous conditions: A dominant feature of the
1279 ocean through Earth's history. *Elements*. 7, 107–112, 2011.

1280 Preuß, A., Schauder, R., Fuchs, G., and Stichler W.: Carbon isotope fractionation by
1281 autotrophic bacteria with three different CO₂ fixation pathways. *Zeitschrift für*
1282 *Naturforschung C.*, 44, 397–402, 1989.

1283 Rancourt, D. G., Fortin, D., Pichler, T., and Lamarche, G.: Mineralogical
1284 characterization of a natural very As-rich hydrous ferric oxide coprecipitate formed
1285 by mixing of hydrothermal fluid and sea water. *Am. Min.*, 86, 834–851, 2001.

1286 Rasmussen, B., Meier, D. B., Krapež. B., and Muhling, J. R.: Iron silicate
1287 microgranules as precursor sediments to 2.5-billion-year-old banded iron
1288 formations. *Geology*, 41, 435–438, 2013.

1289 Rasmussen, B., Krapež, B., and Meier, D. B. Replacement origin for hematite in 2.5
1290 Ga banded iron formation: Evidence for postdepositional oxidation of iron-bearing
1291 minerals. *Geol. Soc. Am. Bull.*, 126, 438–446, 2014.

1292 Riedel, T., Zak, D., Biester, H., and Dittmar, T.: Iron traps terrestrially derived
1293 dissolved organic matter at redox interfaces. *Proc. Nat. Acad. Sci. U.S.A.*, 110,
1294 10101–10105, 2013.

1295 Robbins, E. I., Kourtidou-Papadeli, C., Iberall, A. S., Nord, Jr, G. L. and Sato, M.:
1296 From Precambrian Iron-Formation to Terraforming Mars: The JIMES Expedition
1297 to Santorini. *Geomicrobiol. J.*, 33, 630–645, 2016.

- 1298 Roy, S.: Manganese Mineralization: Geochemistry and mineralogy of terrestrial and
1299 marine deposits. *Geol. Soc. Spe. Pub.*, 119, 5–27, 1997.
- 1300 Roy, S.: Sedimentary manganese metallogenesis in response to the evolution of the
1301 Earth system. *Earth-Sci. Rev.*, 77, 273–305, 2006.
- 1302 Rudnick, R. and Gao, S. Composition of the continental crust. In: *Treatise on*
1303 *Geochemistry*, vol. 3. Elsevier–Pergamon, Oxford, 1–64 pp, 2003.
- 1304 Shanmugam, G.: Submarine fans: a critical retrospective (1950–2015). *J.*
1305 *Palaeogeogr.*, 5, 110-184, 2016.
- 1306 Schwertmann, U. and Murad, E. Effect of pH on the formation of goethite and
1307 hematite from ferrihydrite. *Clay Clay Min.*, 31, 277–284, 1983.
- 1308 Shuster, D. L., Farley, K. A., Vasconcelos, P. M., Balco, G., Monteiro, H. S.,
1309 Waltenberg, K., and Stone, J. O. Cosmogenic ^3He in hematite and goethite from
1310 Brazilian “canga” duricrust demonstrates the extreme stability of these surfaces.
1311 *Earth Plan. Sci. Lett.*, 329, 41–50, 2012.
- 1312 Sigurdsson, H., Carey, S., Alexandri, M., Vougioukalakis, G., Croff, K., Roman, C.,
1313 Sakellariou, D., Anagnostou, C., Rousakis, G., Loakim, C., Goguo, A., Ballas, D.,
1314 Misaridis, T., and Nomikou, P. Marine investigations of Greece’s Santorini
1315 volcanic field. *EOS Trans. Am. Geophys. Union*, 87, 337–342, 2006.
- 1316 Simonson, B. M.: Sedimentological constraints on the origins of Precambrian iron-
1317 formations. *Geol. Soc. Am. Bull.*, 96, 244–252, 1985.
- 1318 Simonson, B. M. and Hassler, S. W.: Was the deposition of large Precambrian iron
1319 formations linked to major marine transgressions? *The J. Geol.*, 104, 665–676,
1320 1996.
- 1321 Skarpelis, N. and Koutles, T.: Geology of epithermal mineralization of the NW part of
1322 Milos Island, Greece. In *Proceedings of the 5th International Symposium on*

1323 Eastern Mediterranean Geology. (eds. Chatzipetros, A. & Pavlides S). School of
1324 Geology, Aristotelian University of Thessaloniki, Thessaloniki, Greece. pp. 1449–
1325 1452, 2004.

1326 Smith, A.J.B., Beukes, N.J., and Gutzmer, J.: The Composition and depositional environments of
1327 Mesoarchean Iron Formations of the West Rand Group of the Witwatersrand Supergroup, South
1328 Africa. *Econ. Geol.* 108, 111-134, 2013.

1329 Sperling, E.A., Wolock, C.J., Gill, B.C., Kunzmann, M., Halverson, G.P., Macdonald,
1330 F.A., Knoll, A.H., and Johnston D.T.: Statistical Analysis of Iron Geochemical
1331 Data Suggests Limited Late Proterozoic Oxygenation. *Nature* 523, 451–454, 2015.

1332 Stewart, A. L. and Mcphie, J.: Facies architecture and Late Pliocene – Pleistocene
1333 evolution of a felsic volcanic island, Milo, Greece. *Bull. Volcanol.* 68, 703–726,
1334 2006.

1335 Sun, S., Konhauser, K. O., Kappler, A., and Li, Y.-L.: Primary hematite in
1336 Neoproterozoic to Paleoproterozoic oceans. *GSA Bull.*, 127, 850–861, 2015.

1337 Stüben, D. and Glasby, G.P.: Geochemistry of shallow submarine hydrothermal fluids
1338 from Paleohori Bay, Milos, Aegean Sea. *Exp. Min. Geol.*, 8, 273–287, 1999.

1339 Swamy, V., Saxena, S. K., Sundman, B., and Zhang, J.: A thermodynamic assessment
1340 of silica phase diagram. *J. Geophys. Res. Solid Earth*, 99, 11787–11794, 1994.

1341 Taylor, J., and Parkes, R. J.: The cellular fatty-acids of the sulfate-reducing bacteria,
1342 *Desulfobacter* sp., *Desulfobulbus* sp. and *Desulfovibrio desulfuricans*. *J. Gen.*
1343 *Microbiol.*, 129, 3303–3309, 1983.

1344 Tice, M. M. and Lowe, D. R.: The origin of carbonaceous matter in pre-3.0 Ga
1345 greenstone terrains: A review and new evidence from the 3.42 Ga Buck Reef
1346 Chert. *Earth Sci. Rev.*, 76, 259–300, 2006.

1347 Tiodjio, R. M., Sakatoku, A., Nakamura, A., Tanaka, A., Fantong, W. Y., Tchakam,
1348 K. B., Tanyileke, G., Ohba, T., Hell, V. J., Kusakabe, M., Nakamura, S., and Ueda,

1349 A.: Bacterial and archaeal communities in Lake Nyos (Cameroon, Central Africa).
1350 Sci. Rep., 4, 6151, DOI: 10.1038/srep06151, 2014.

1351 Trendall, A.F.: The significance of iron-formation in the Precambrian stratigraphic
1352 record. *Int. Assoc. Sed. Spe. Pub.*, 33, 33–66, 2002.

1353 Tsikos, H., Mathews, A., Erel, Y., and Moore, J.M.: Iron isotopes constrain
1354 biogeochemical redox cycling of iron and manganese in a Palaeoproterozoic
1355 stratified basin. *Earth Planet. Sci. Lett.*, 298, 125–134, 2010.

1356 van Hinsbergen, D. J. J., Snel, E., Garstman, S. A., Mărunțeanu, M., Langereis, C. G.,
1357 Wortel, M. J. R., and Meulenkamp, J. E.: Vertical motions in the Aegean volcanic
1358 arc: evidence for rapid subsidence preceding volcanic activity on Milos and
1359 Aegina. *Mar. Geol.*, 209, 329–345, 2004.

1360 Varnavas, S. P. and Cronan, D. S.: Submarine hydrothermal activity off Santorini and
1361 Milos in the Central Hellenic Volcanic Arc: A synthesis. *Chem. Geol.*, 224, 40–54,
1362 2005.

1363 Weber, K. A., Achenbach, L. A., and Coates, J. D.: Microorganisms pumping iron:
1364 anaerobic microbial iron oxidation and reduction. *Nat. Rev. Microbiol.*, 4, 752–64,
1365 2006.

1366

1367

1368

1369

1370

1371

1372

1373

1374

1375

1376

1377

1378

1379

1380

1381

1382

1383

1384

1385 Table 1. Table 1. Results of X-Ray Radiation (XRD) analysis showing major
 1386 mineralogical compositions. NFIF (non-fossiliferous iron formation) and MFIF
 1387 (microfossiliferous iron formation), respectively.

1388

Mineral phase	MFIF1	MFIF2	MFIF3	Fe-rich NFIF2A	Si-rich NFIF2B	Fe-rich NFIF2C	Si-rich NFIFD	Fe-rich NFIF2E	Fe-rich NFIF2F
Hematite	+	+	-	+	+	+	+	+	+
Quartz	+	+	+	-	-	-	-	-	-
Sanidine	-	-	-	+	+	+	+	+	+
Tridymite	-	-	-	-	+	+	+	+	+
Cristobalite	-	-	-	+	-	-	-	-	-
Cryptomelane	-	-	+	-	-	-	-	-	-

1389

1390

1391

1392

1393

1394

1395

1396

1397

1398

1399

1400

1401

1402

1403
 1404
 1405
 1406
 1407
 1408
 1409
 1410
 1411
 1412
 1413
 1414
 1415
 1416
 1417
 1418
 1419
 1420
 1421
 1422

Table 2. Stable isotope results. Letters A-F on the NFIF samples represent respective bands of the sawn rock in Figure 7E.

Sample	$\delta^{13}\text{C}_{\text{org}}$ vs PDB (‰)	C_{org} (%)	$\delta^{15}\text{N}$ vs air (‰)	N (%)	$\delta^{34}\text{S}$ vs CDT (‰)	S (%)
Fe-rich NFIF2A	-25,63	0,061	nd	0,023	nd	0,01
Si-rich NFIF2B	-25,03	0,109	nd	0,017	nd	0,02
Fe-rich NFIF2C	-24,45	0,068	nd	0,013	nd	0,02
Si-rich NFIF2D	-25,04	0,076	nd	0,015	nd	0,02
Fe-rich NFIF2E	-25,19	0,042	nd	0,009	nd	0,01
Si-rich NFIF2F	-25,49	0,050	nd	0,012	nd	0,03
MFIF1	-25,49	0,087	nd	0,017	nd	0,01
MFIF2	-26,25	0,046	nd	0,005	nd	nd
MFIF3	-25,69	0,041	nd	0,006	nd	nd

ND, Not detected

1424
 1425
 1426
 1427
 1428
 1429
 1430
 1431

 1432

 1433

1434

1435

1436

1437

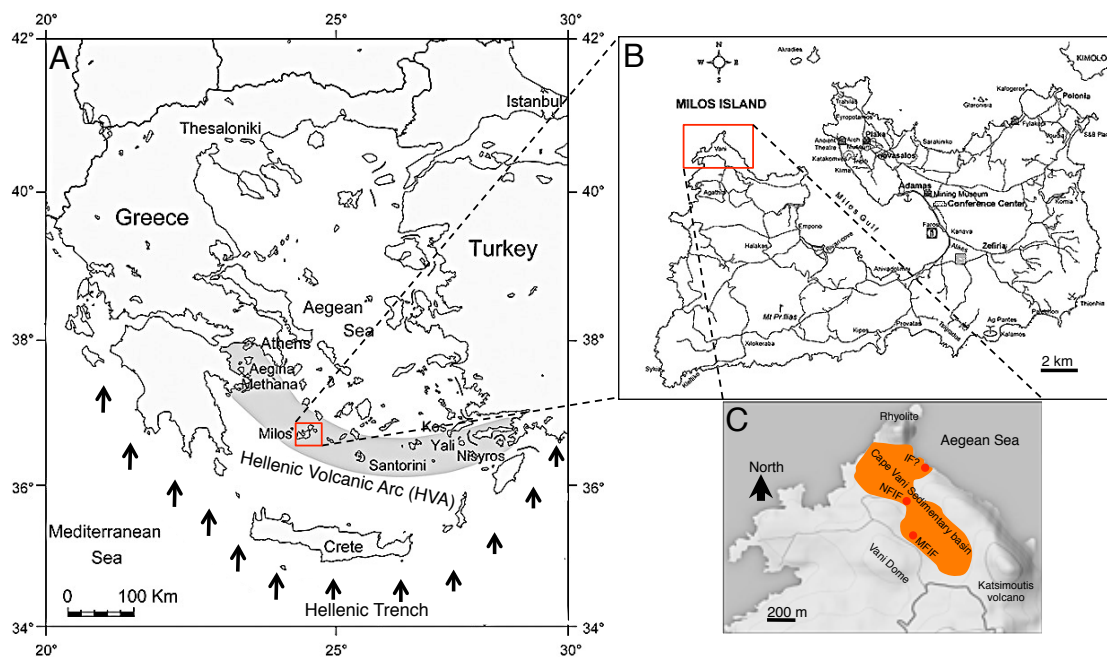
1438

1439

1440

1441

1442

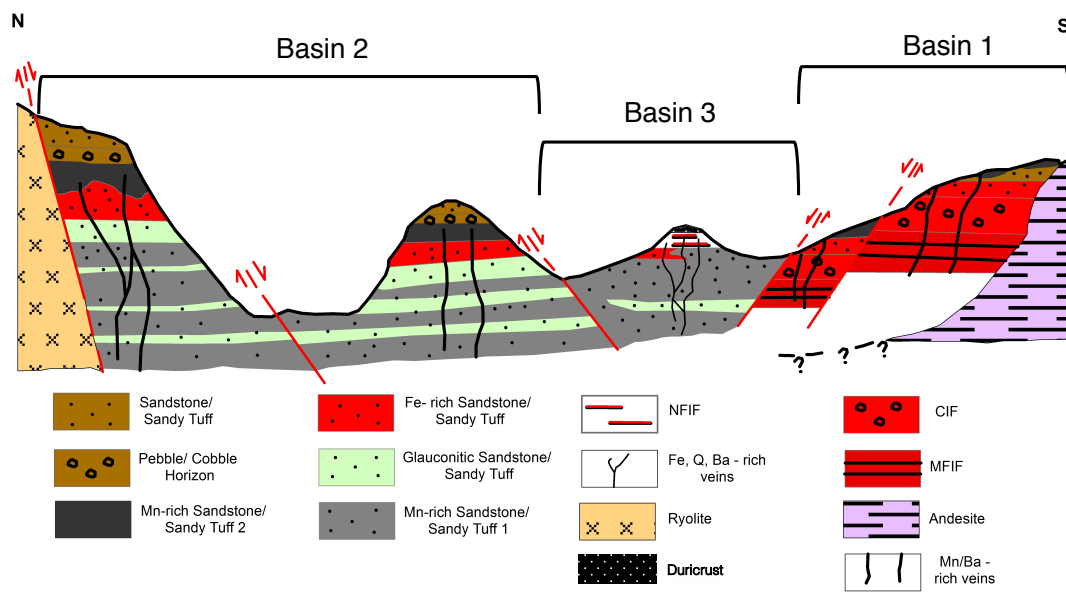


1443

1444 Fig. 1. Geological map of Milos (redrawn from Marschik et al., 2010). (A),
1445 Geotectonic map showing the position of Milos Island, along the Hellenic Volcanic
1446 Arc (HVA). Arrows indicate north east subduction of the African plate underneath the
1447 Eurasian plate. (B) Milos Island. (C), The Milos iron formation is located in the 8-
1448 shaped Cape Vani sedimentary basin (CVSB). At least two IFs are present in the
1449 CVSB. These are made up of a non-fossiliferous IF (NFIF) at the juncture between
1450 the two large sedimentary basins and a microfossiliferous IF (MFIF) located at the
1451 SW margin in the second basin. A potential third IF (IF?) is located to the NE, close
1452 to the present day Aegean Sea. It is however not certain if this deposit is part of the
1453 NFIF or not, because of the open mining pit separating the two.

1454

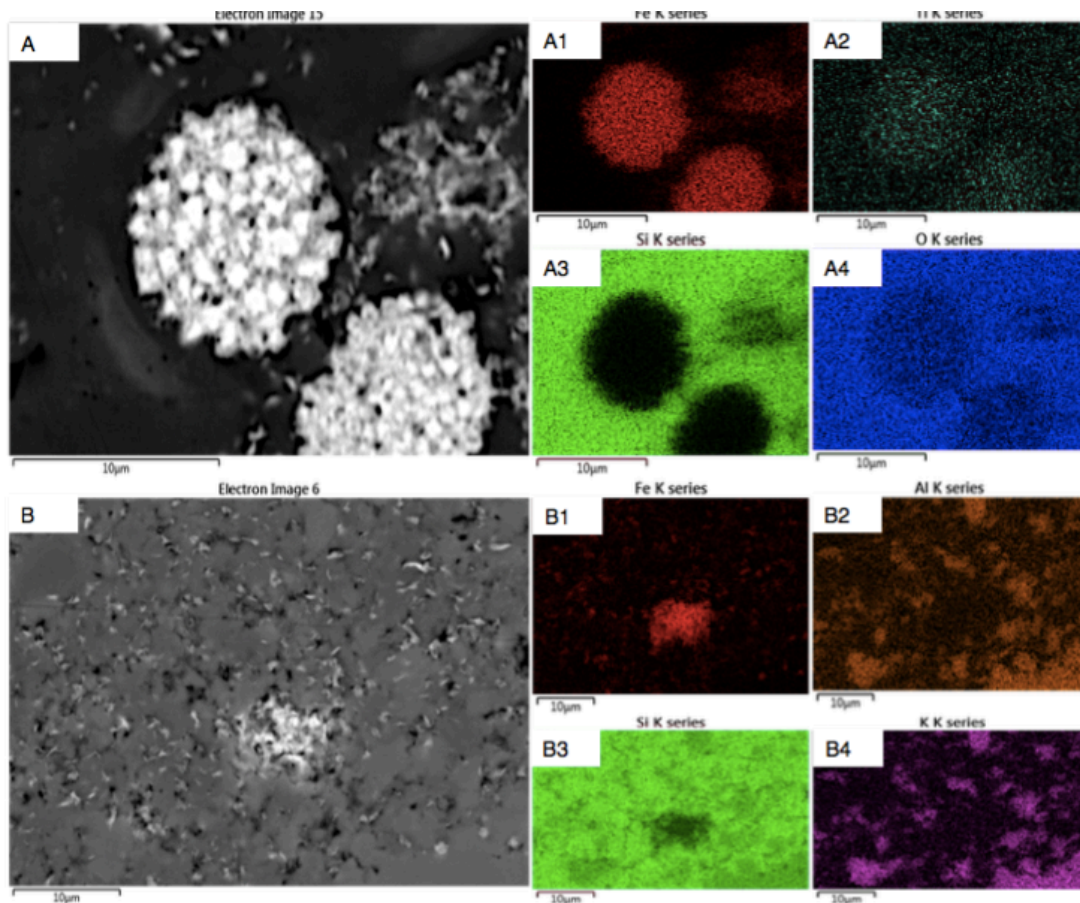
1455



1456

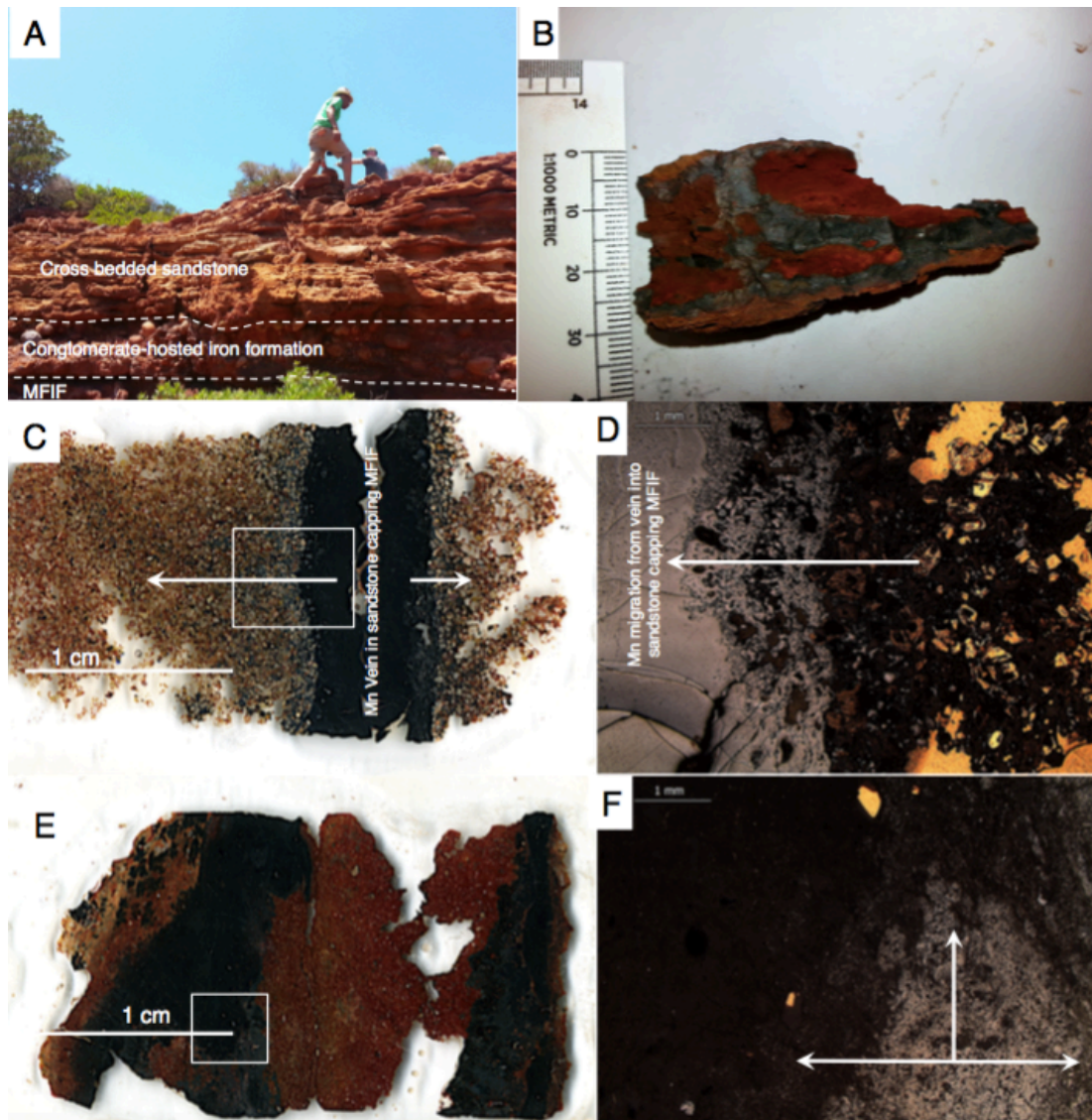
1457 Fig. 2. A generalized north-south stratigraphic map of the ~1 km long CVSB showing
 1458 interpreted geology, lithology, main faults and how they relate to the iron and
 1459 manganese formations, in support of a three-basin hypothesis. Not drawn to scale.
 1460 Four types of iron-rich sedimentary rocks occur in the CVSB. These include the iron-rich
 1461 sandstones, the iron-Mn-rich sandstones, the conglomerate hosted iron formation
 1462 (CIF) and the MFIF and NFIF formations that are depositionally and chemically
 1463 distinct from the sandstone deposits.
 1464

1465



1466

1467 Fig. 3. EDS-electron micrograph showing Fe-rich mineral phases in a Si-rich matrix
 1468 from the MFIF. The bright colors correspond to the analysed elements. (A),
 1469 framboidal hematite particles. A1-A4, elemental compositions of the framboidal
 1470 particles in A. (B), Dispersed fluffy Fe-rich mineral grains. B1-B4, corresponding
 1471 elements associated with the micrograph in panel A
 1472

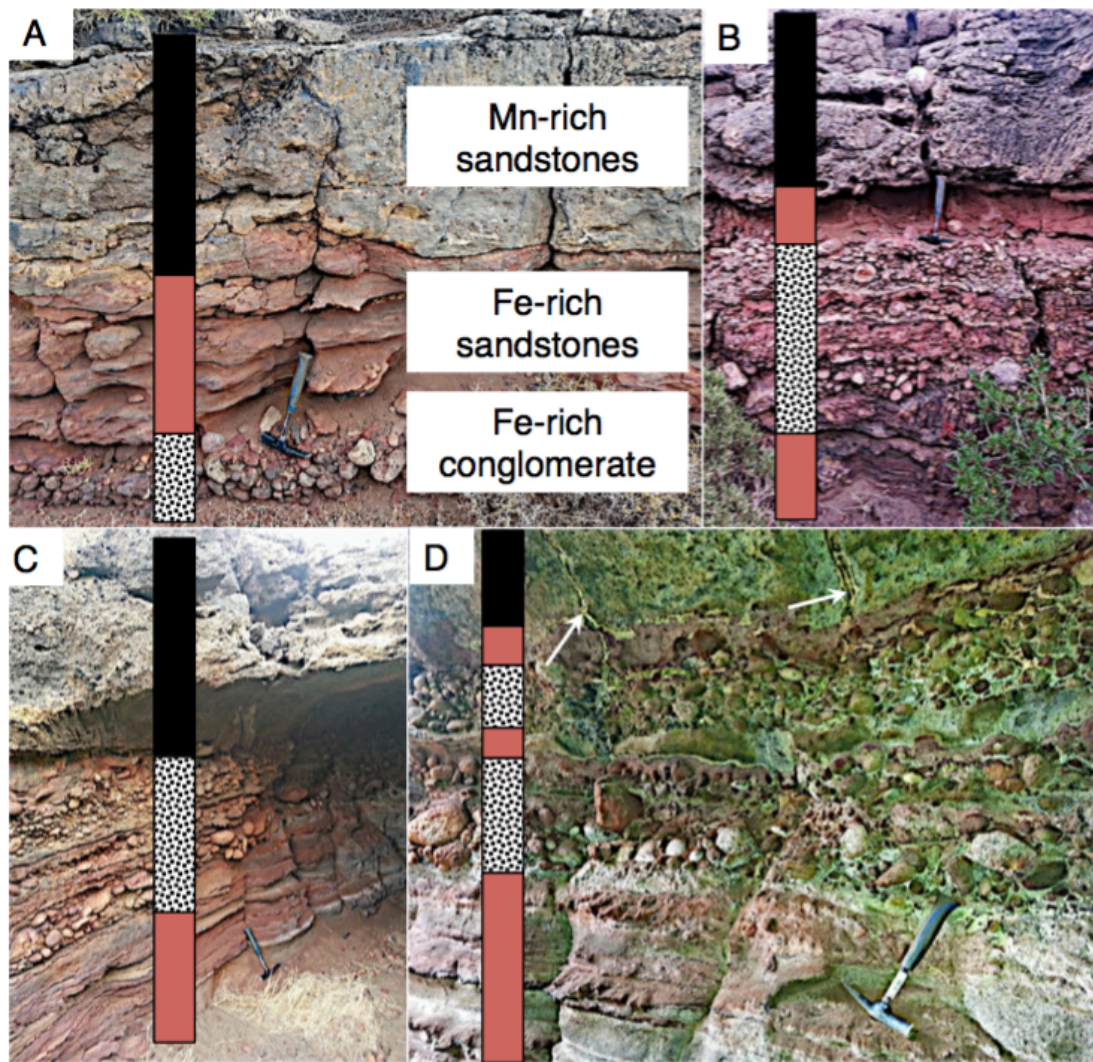


1473

1474 Fig. 4. Sedimentary profile, thin section scans and optical microscope images of the
 1475 MFIF. (A), Field photo showing the sedimentary profile of the MFIF characterized by
 1476 the overlying sandstone cap. (B), Photograph showing black diffused Mn-rich bands
 1477 near the base of the MFIF. (C), Scanned image of thin section showing a black Mn-
 1478 rich vein in the overlying MFIF sandstone showing a gradient of Mn migrating into
 1479 the sandstone matrix (white arrows). (D), Light microscopy images showing details in
 1480 panel C. (E), Scanned image of an MFIF thin section showing black Mn bands
 1481 migration into a red iron-rich background. (F), Amplified light microscope image
 1482 showing gray Mn layers migrating into a black Fe-rich matrix. White arrows show
 1483 direction of movement. Boxes in C and E are amplified in D and F.

1484

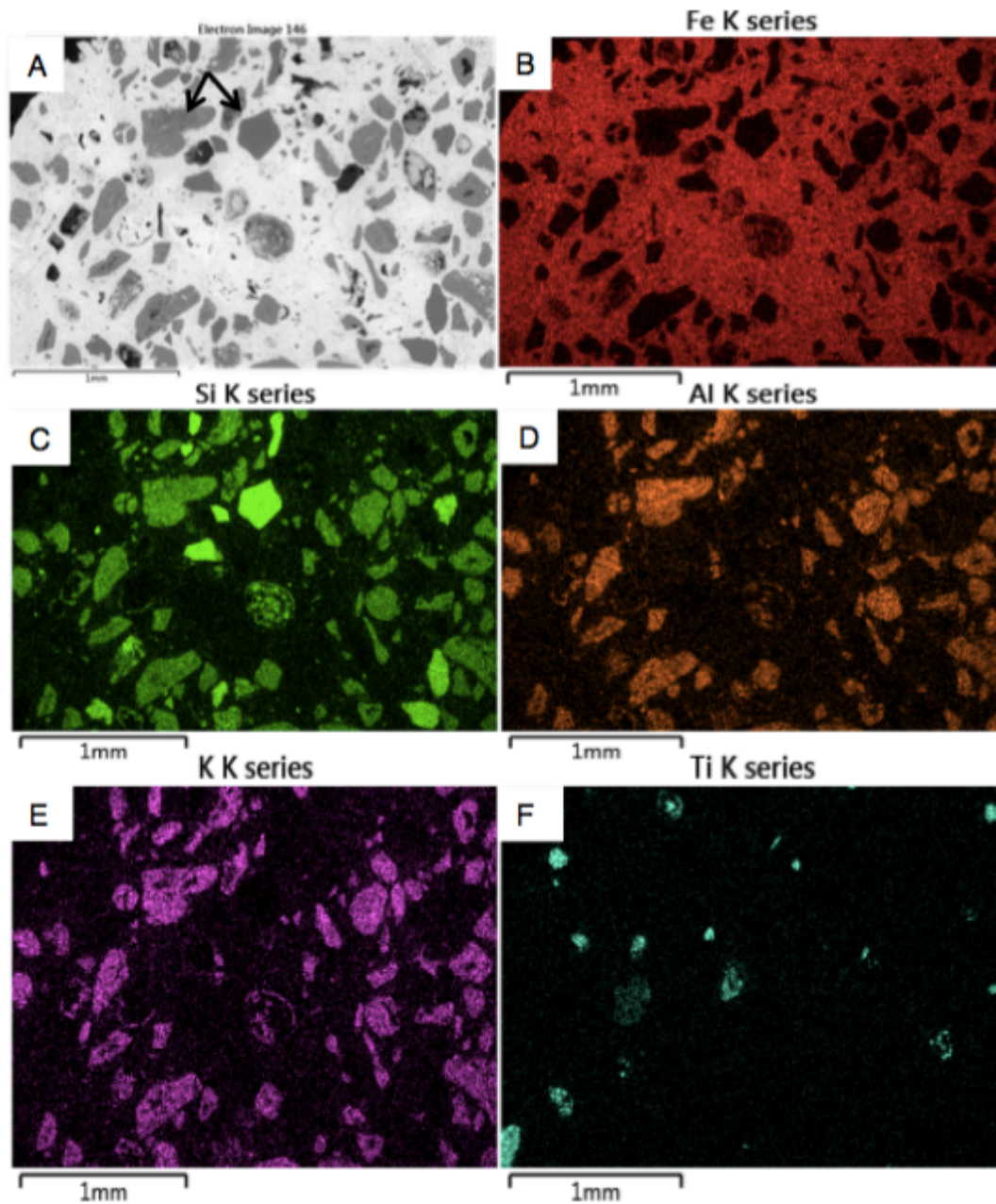
1485



1486

1487 Fig. 5. Sedimentary sequence overlying the MFIF, consisting of thin (<0.5 m)
 1488 polymictic andesite-dacite cobble-pebble, and sandstone-sandy tuff pebble, and Fe-
 1489 rich conglomerate facies overlain by thinly laminated Fe-rich sandstone beds. This
 1490 vertical sequence is interpreted to represent a progressively deeper water environment
 1491 up the sequence (A), for reasons including sea level rise due to tectonic subsidence.
 1492 The multiple cycles in B-D suggest potential episodes of sea level change. Arrows in
 1493 D show hydrothermal feeder veins feeding the overlying layers. The sequence is
 1494 overlain by a thin package of parallel and cross-bedded Mn-sandstone cap.
 1495

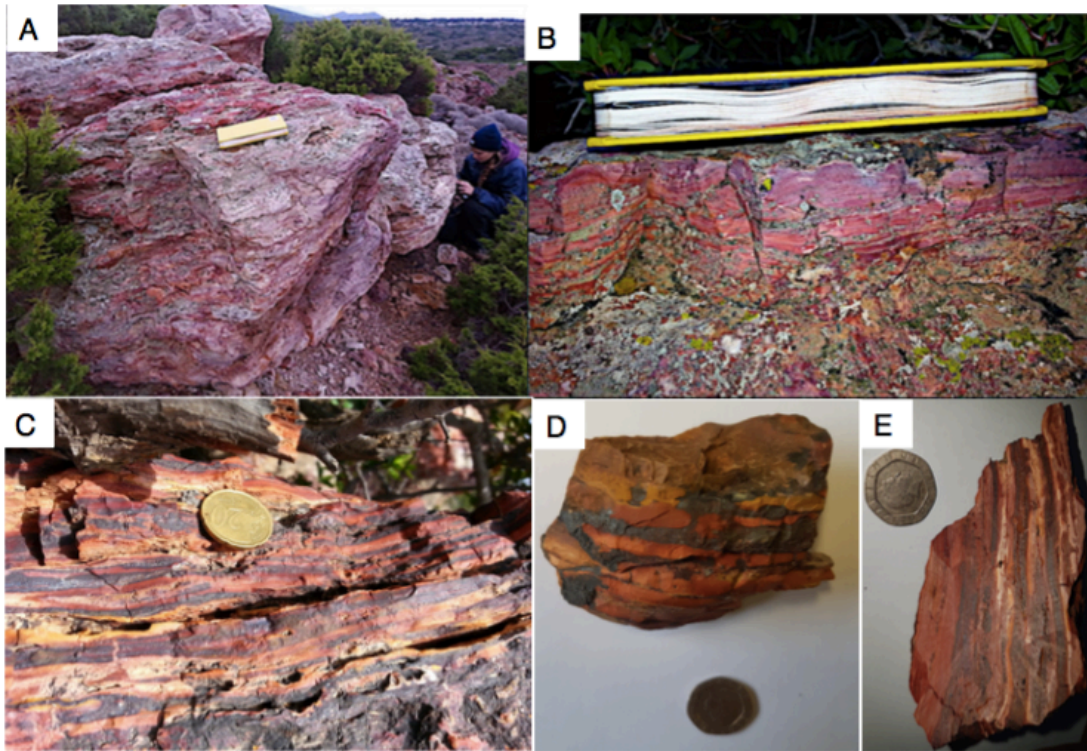
1496



1497

1498 Fig. 6. Scanning electron microscope micrograph showing the chemical composition
 1499 of volcaniclast (arrows in A) and the iron cement of the conglomerate hosted IF (CIF)
 1500 overlying the MFIF.
 1501

1502

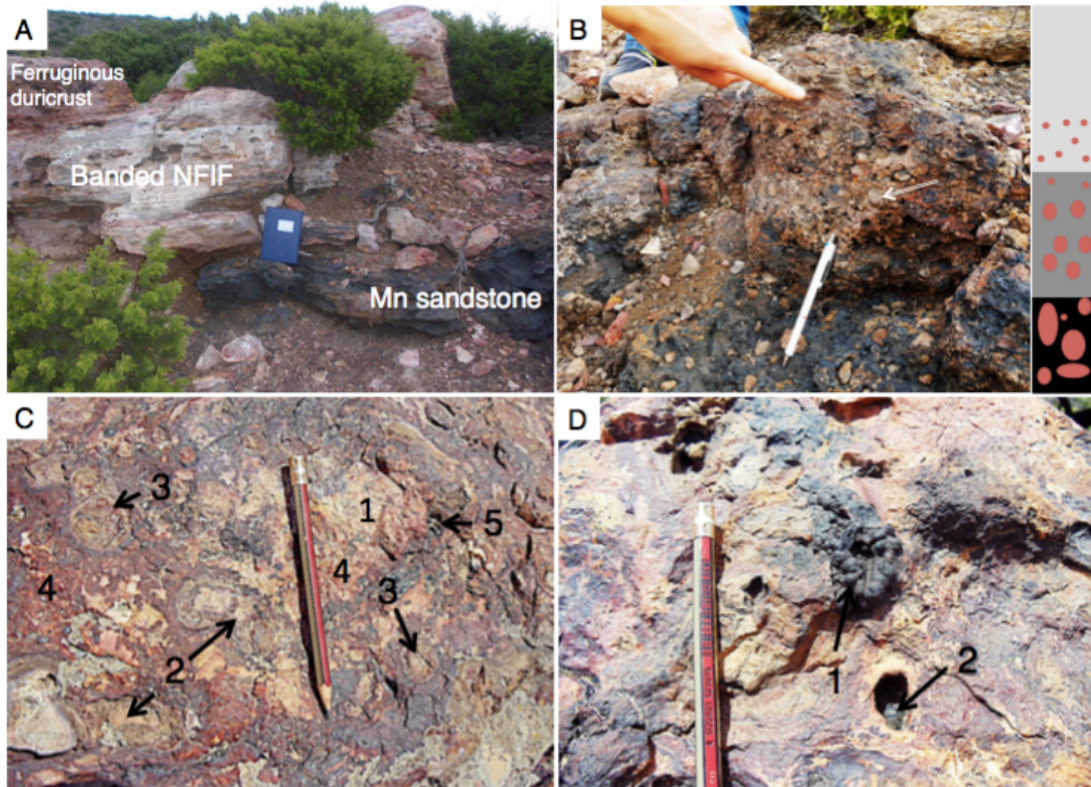


1503

1504 Fig. 7. Examples of the NFIF banded iron rocks. (A-C), Field photographs. (D),
1505 Handheld banded Fe sample. (E), Sawn NFIF sample with laminated Fe-rich bands
1506 alternating with Si-rich bands.

1507

1508

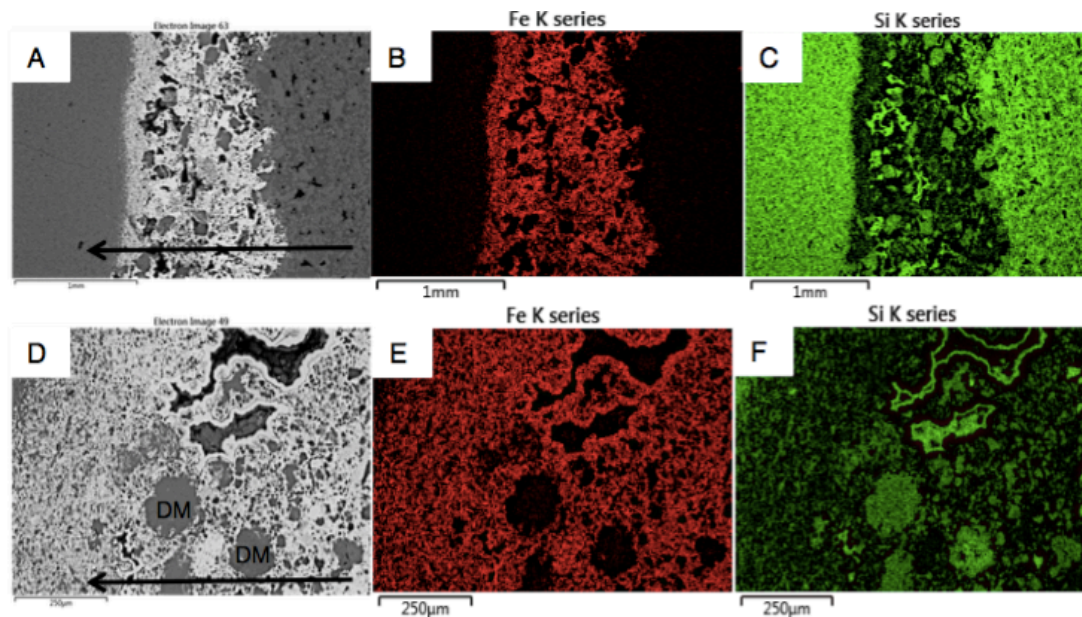


1509

1510 Fig. 8. Field sedimentology and stratigraphy of Section B sequence, host to the NFIF.
 1511 (A), Sharp boundary between lower Mn sandstone and unconformably overlying
 1512 NFIF capped by a ferruginous duricrust. (B), Sandstone-sandy tuff pebble to gravel
 1513 conglomerate facies, showing an upward fining character, locally overlies the Mn
 1514 sandstone bed and capped by a sharp erosional contact with the overlying NFIF. The
 1515 tip of the pen (7 cm long) rests on late blue-black Mn oxide overprint. (C),
 1516 Ferruginous duricrust made up of lithic fragments composed of (1) Fe-nodules (2) and
 1517 Fe-concretions (3) in a hematite-rich matrix (4). (D), Matrix dissolution resulting in
 1518 vermiform Mn nodules (1) and cavity black Mn oxide (2) infillings, post-dating the
 1519 ferruginous duricrust formation.

1520

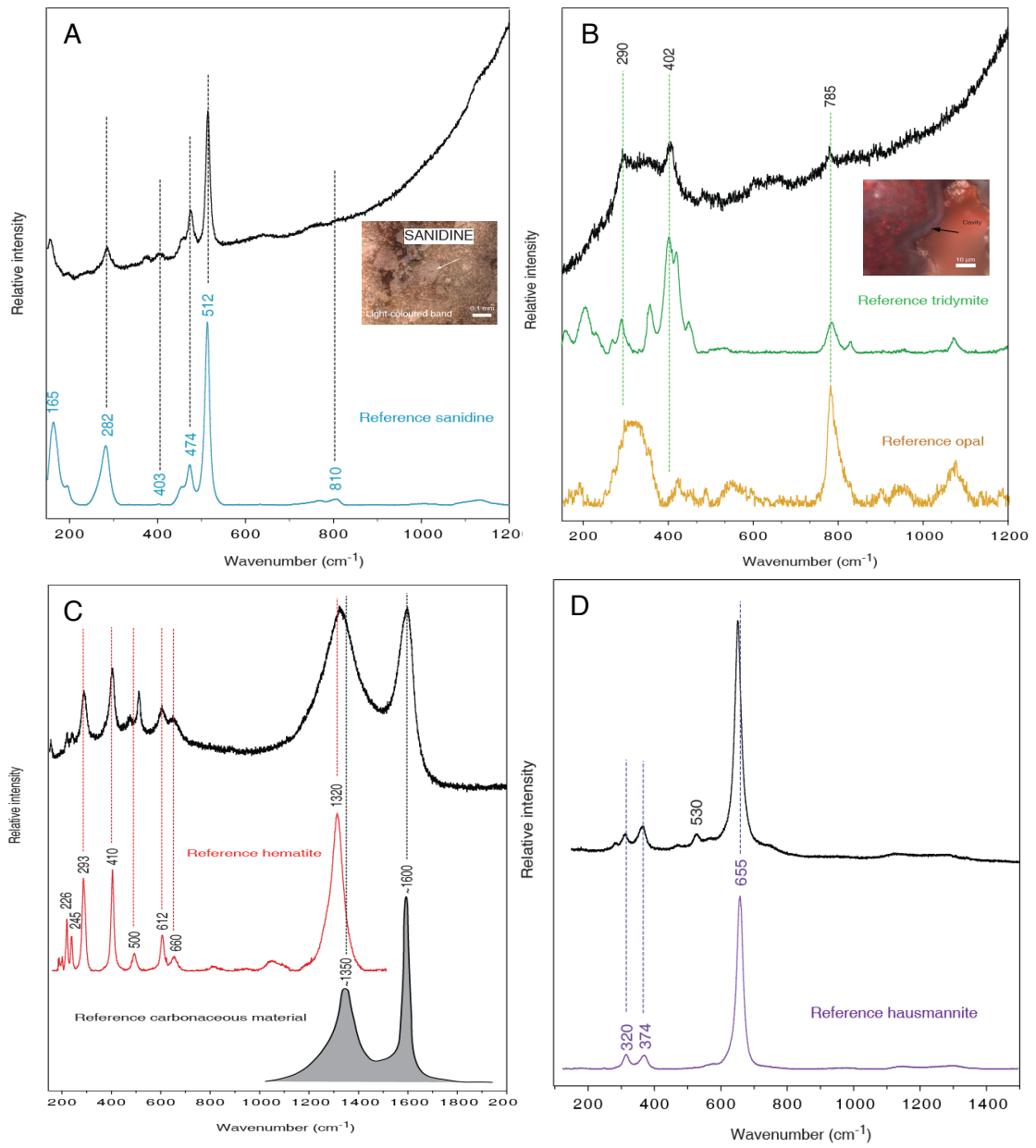
1521



1522

1523 Fig. 9. EDS-electron micrograph showing major elemental composition of typical Fe
 1524 bands alternating with Si-rich layers in the NFIF. Volcaniclastic detritus mostly
 1525 present in the Fe-rich bands, suggests precipitation during active submarine
 1526 volcanism. To the contrary, the Si-rich band grains that are of a homogenous fine size
 1527 composition and lacking volcaniclast, suggest deposition during intervals of minimal
 1528 volcanic activity. Arrows in A and B depict the direction of sedimentation, seen to
 1529 proceed from an Fe-rich matrix mixed with large grains of volcaniclastic detritus
 1530 (DM) to one composed essentially of very fine-grained Fe particles before
 1531 transitioning into the very fine-grained Si-rich layer. An upward fining of the
 1532 volcaniclastic particles in the Fe-rich layers transitions from one made up of
 1533 volcaniclastic debris and hematite, to a mainly thin hematite-rich horizon at the top of
 1534 this mixed layer (see supplementary Figs 8-11 for details). This concurrent occurrence
 1535 of volcaniclast and Fe oxides, combined with the upward fining nature of the Fe-rich
 1536 layers, suggest the release and oxidation of Fe(II) coincided with the settling of
 1537 hydrothermal debris resulting from the introduction of enormous amount of reduced
 1538 materials into the water column. The Fe-rich layer ceased forming as
 1539 hydrothermal/volcanic release of Fe subsided, followed by deposition of the Si-rich
 1540 layer. This repetitive cycle of events is observed for tens of metres laterally and
 1541 vertically, stressing that the layers are not single isolated or post-depositional
 1542 replacement events, but chemical precipitates that sequentially sedimented out of the
 1543 water column. Red color in B and C depict Fe and green in C and F, Si.
 1544

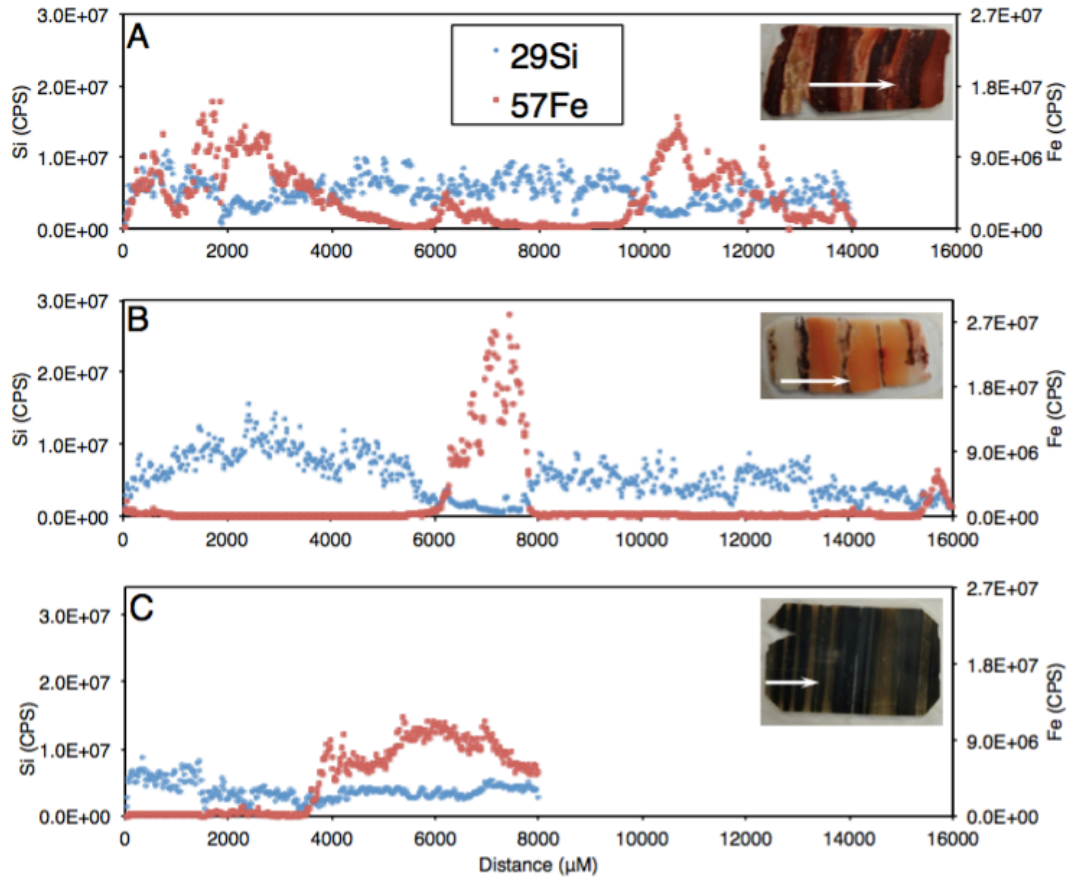
1545



1546

1547 Fig. 10. Raman spectroscopy of the Fe-rich and/or Si-rich bands from NFIF.

1548

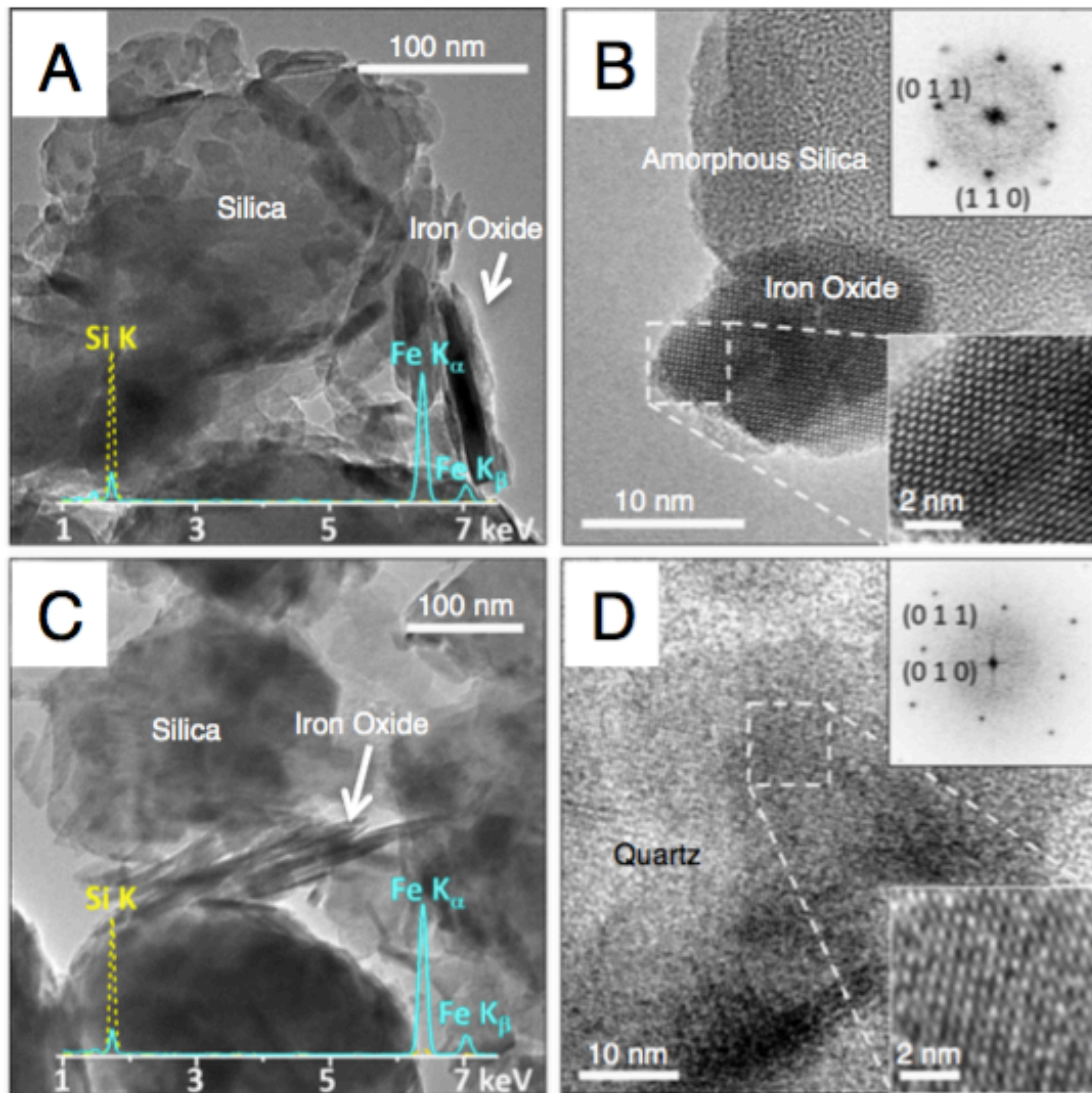


1549

1550 Fig. 11. Fluctuation in Si and Fe content measured by in situ laser ablation ICP-MS
 1551 analysis. (A), Milos BIF-type rock with evenly distributed Si and Fe rich bands. (B),
 1552 Milos BIF type rock with wide Si-rich (whitish-brownish strips) and narrow Fe-rich
 1553 bands (dark strips). (C), An example for the 2.5 Ga Kuruman BIF. Insets are analyzed
 1554 thin sections. For scale, each thin section is ≈ 3.3 cm long, in the direction of the
 1555 arrows indicating the area analyzed.

1556

1557



1558

1559 Fig. 12. TEM characterization of an NFIF and MFIF specimen. (A) lower
 1560 magnification MFIF TEM-BF micrograph. (B) High resolution micrograph of NFIF
 1561 showing amorphous Si and Fe oxide crystalline lattice structures. Insets highlight a
 1562 hematite particle viewed from the [1-11] axis (Rhombohedral lattice). (C) Lower
 1563 magnification MFIF TEM-BF image. (D) High resolution images of MFIF showing
 1564 crystalline quartz and iron oxide crystalline lattice structures. Insets in (D) show a
 1565 quartz crystal viewed from the [100] axis. Both samples contain silica with a few
 1566 hundred nm particle size, and smaller needle-like iron oxide particles. Spectral lines
 1567 in panels (A) and (C) are X-ray Energy Dispersive elemental profiles of the individual
 1568 Fe and Si mineral phases.

1569

1570

1571

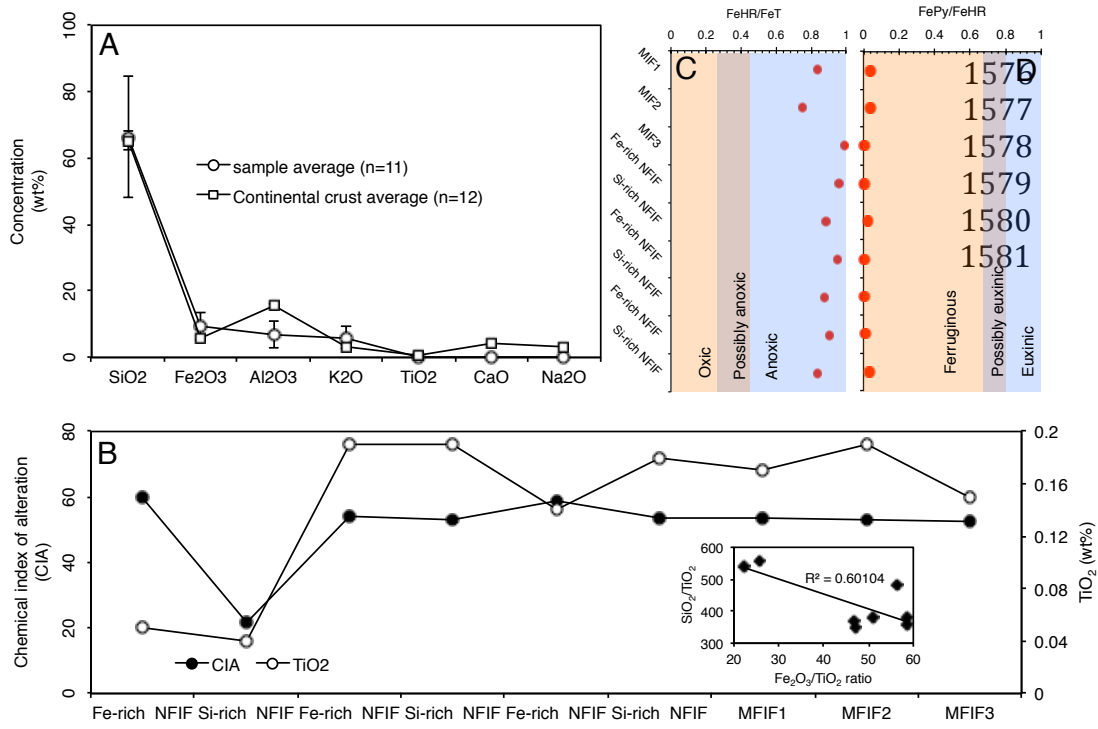
1572

1573

1574

1575

1582
1583
1584
1585



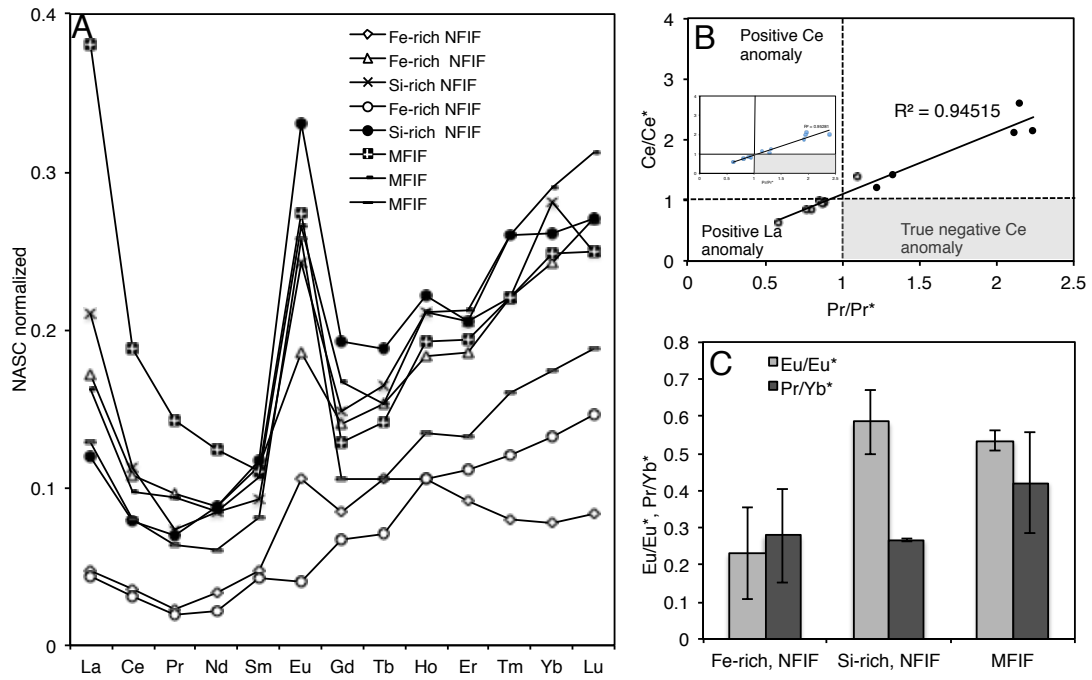
1586
1587
1588
1589
1590
1591
1592
1593
1594
1595
1596

Fig. 13. Bulk average concentrations of major trace elements, chemical weathering indices and reconstructed redox depositional conditions for typical MFIF and the Fe/Si-rich NFIF ands for the sawn rock sample in Figure 7E. (A), Relationship between average major trace element content and average continental crust (Rudnick and Gao, 2003). (B), Chemical Index of Alteration (CIA). Inset, relationship between SiO_2 and Fe_2O_3 . (C) Highly reactive Fe (FeHR) to Total Fe ratio (FeT). (D) Pyrite to FeHR ratio.

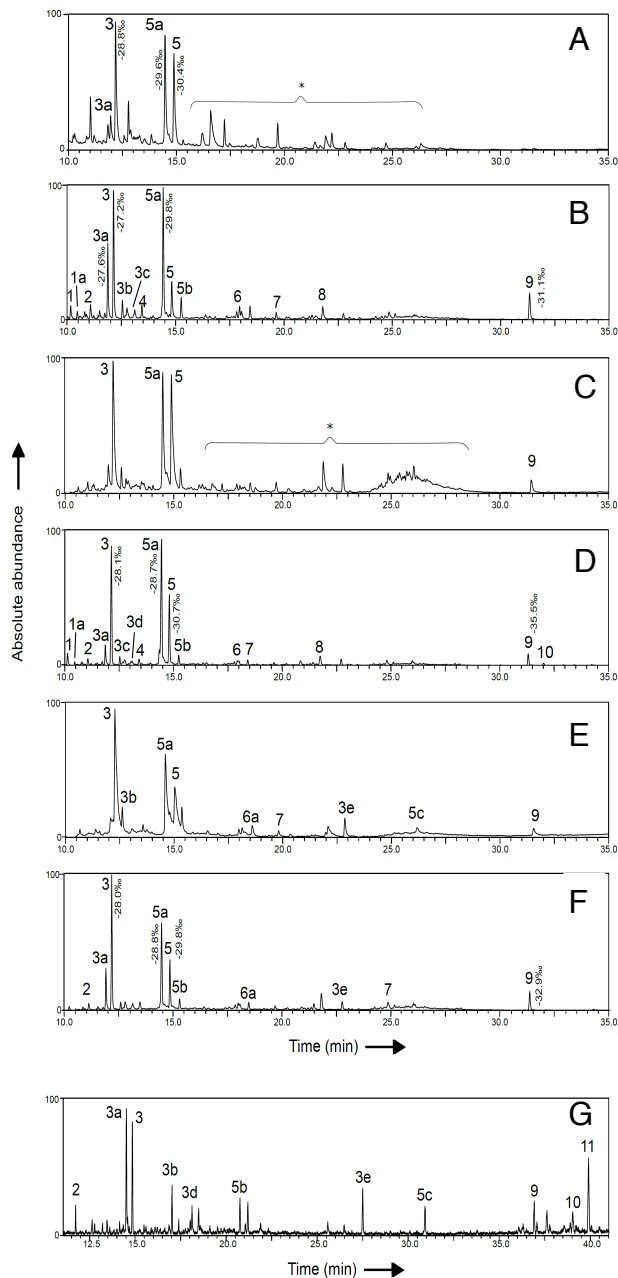
1597
1598
1599
1600
1601
1602
1603
1604
1605

1606

1607



1608 Fig. 14. Rare earth element (REE) distribution in samples and calculated Ce and Eu
 1609 anomalies for NFIF bands and MFIF. (A), NASC normalized REE distribution in
 1610 various rock facies. (B), Ce anomalies. (C), Eu anomalies and light REE (LREE) vs.
 1611 heavy REE (HREE) ratio in the NFIF bands and MFIF. Similar trends were
 1612 reproduced for Post Archean Australian Shale (PAAS) normalized REE (McLennan,
 1613 1989; Bau and Dulski, 1986), exemplified by the inset in B.



1614

1615 Fig. 15. GC/MS chromatogram sections of total lipid extracts of the BIF-type rocks
 1616 (A-F). Data are for individual bands excised from the sawn rock in Figure 7E. Panel
 1617 G illustrates total lipid extract for the modern shallow submarine hydrothermal
 1618 sediments at Spathi Bay, south east on the coast of Milos Island. Peak values indicate
 1619 the lipid-specific $\delta^{13}\text{C}$ values per mil. Because of the low intensity of the lipids
 1620 recovered, it was not possible to obtain $\delta^{13}\text{C}$ values specific for all peaks. Peaks are
 1621 annotated as; FAME = fatty acid methyl ester; Me = methyl group; TMS =
 1622 trimethylsilyl; TMSE = trimethylsilyl ester. (1) $\text{C}_{14:0}$ FAME, (1a) $\text{C}_{14:0}$ 13Me FAME,
 1623 (2) $\text{C}_{15:0}$ FAME, (3) $\text{C}_{16:0}$ FAME, (3a) $\text{C}_{16:9}$ FAME, (3b) $\text{C}_{16:0}$ TMS, (3c) 10Me $\text{C}_{16:0}$
 1624 FAME, (3d) $\text{C}_{16:9}$ FAME, (3e) $\text{C}_{16:0}$ TMSE, (4) $\text{C}_{17:0}$ TMS, (5) $\text{C}_{18:0}$ FAME, (5a) $\text{C}_{18:9}$

1625 FAME, (5b) C_{18:0} TMS, (5c) C_{18:0} TMSE, (6) C_{19:0} FAME, (6a) C_{19:0} 18Me TMS, (7)
1626 C_{21:0} TMS, (8) C_{22:0} TMS, (9) Cholesterol TMS, (10) Stigmasterol TMS, (11) beta-
1627 Sitosterol (*) contaminants (e.g., phthalates).
1628

1629

1630

1631

1632

1633

1634

1635

1636

1637

1638

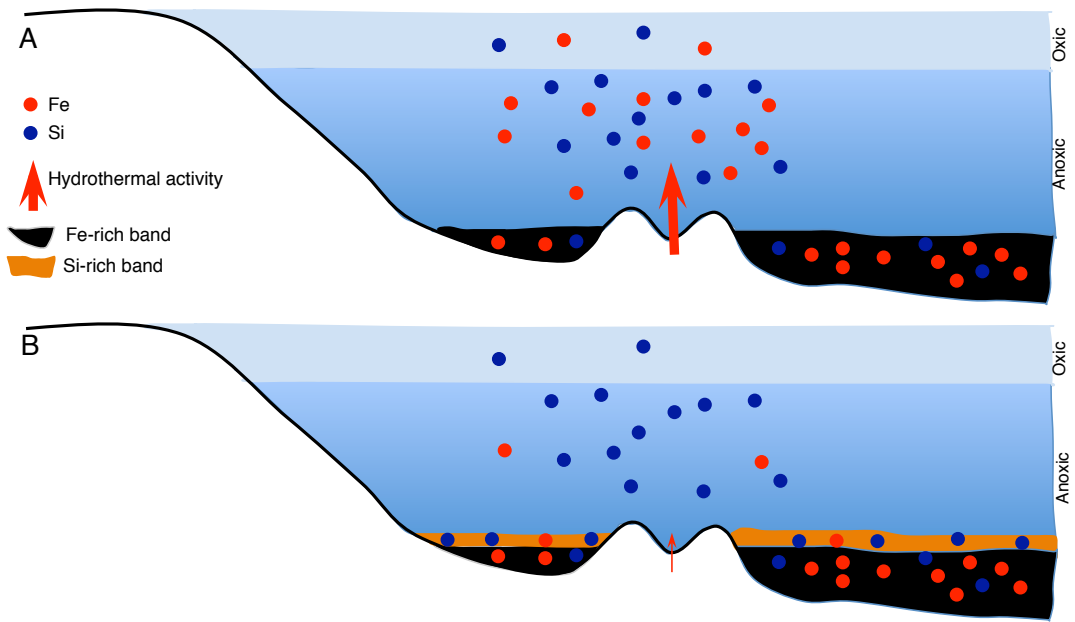
1639

1640

1641

1642

1643



1644

1645 Fig. 16. Conceptual model of the mechanism of band formation of the NFIF, related
 1646 to changes in the intensity of hydrothermal activity and chemical oxidation of Fe(II)
 1647 to Fe(III) in the water column, inferred from the data. See Chi Fru et al. (2013) for a
 1648 biological model for the formation of the MFIF.